

1-1-2008

Effects Of Grain Geometry And Vibration On The Suppression Of Combustion Instability In A Solid Rocket Motor

Christopher Baczynski
Ryerson University

Follow this and additional works at: <http://digitalcommons.ryerson.ca/dissertations>

 Part of the [Aerospace Engineering Commons](#)

Recommended Citation

Baczynski, Christopher, "Effects Of Grain Geometry And Vibration On The Suppression Of Combustion Instability In A Solid Rocket Motor" (2008). *Theses and dissertations*. Paper 1076.

This Thesis is brought to you for free and open access by Digital Commons @ Ryerson. It has been accepted for inclusion in Theses and dissertations by an authorized administrator of Digital Commons @ Ryerson. For more information, please contact bcameron@ryerson.ca.

TL
784
CG
EHL
2008

**EFFECTS OF GRAIN GEOMETRY AND VIBRATION ON THE
SUPPRESSION OF COMBUSTION INSTABILITY IN A SOLID
ROCKET MOTOR**

by

Christopher Baczynski

B.A.Sc., Engineering Science - Aerospace, University of Toronto, Toronto,
2000

A thesis
presented to Ryerson University
in partial fulfilment of the
requirements for the degree of
Master of Applied Science
in the program of
Aerospace Engineering

Toronto, Ontario, Canada, 2008
© (Christopher Baczynski) 2008

I hereby declare that I am the sole author of this thesis.

I authorize Ryerson University to lend this thesis to other institutions or individuals for the purpose of scholarly research.

Christopher Baczynski

I further authorize Ryerson University to reproduce this thesis by photocopying or by other means, in total or in part, at the request of other institutions or individuals for the purpose of scholarly research.

Christopher Baczynski

Ryerson University requires the signature of all persons using or photocopying this thesis.
Please sign below, and give address and date.

EFFECTS OF GRAIN GEOMETRY AND VIBRATION ON THE SUPPRESSION OF COMBUSTION INSTABILITY IN A SOLID ROCKET MOTOR

Christopher Baczynski

MASc, Aerospace Engineering, Ryerson University, Toronto, 2008

Abstract

A comprehensive numerical model for internal ballistic simulation under dynamic flow, combustion and structural vibration conditions is used to investigate the effectiveness of grain port area transitions of a reference solid rocket motor as a means for suppression of axial combustion instability symptoms. Modification of the propellant grain geometry is one of several traditional means for suppressing symptoms in actual motors. With respect to these symptoms, individual transient simulation runs show the evolution of the axial pressure wave and associated DC shift for the given grain geometry, as initiated by a given pressure disturbance. Limit pressure wave magnitudes are collected for a number of simulation runs for different grain area transition positions, steepness and aspect ratios, and mapped on an attenuation trend chart. Effects of acceleration, through structural vibration of the propellant surface, on the combustion process are investigated, and their influence on the effectiveness of grain area transitions is examined. With or without acceleration/vibrations effects included, the numerical results produced in this study confirm the significant ability of a grain area transition to suppress combustion instability symptoms.

Acknowledgements

Foremost, I would like to thank Dr. David R. Greatrix, my thesis supervisor, for giving me the opportunity to study in this exciting field. No research is created out of a vacuum, and it is his work that paved the way for the present thesis. I would also like to thank my family and my fiancée for their moral support and words of encouragement.

Table of Contents

| | |
|--|-------------|
| Abstract..... | v |
| Acknowledgements..... | vi |
| Table of Contents..... | vii |
| List of Tables..... | ix |
| List of Figures..... | x |
| Nomenclature..... | xiii |
| | |
| 1 Introduction..... | 1 |
| 1.1 Background..... | 1 |
| 1.2 Objective..... | 2 |
| 1.3 Approach and Computational Model..... | 2 |
| | |
| 2 Fluid Dynamics and Combustion Considerations..... | 5 |
| 2.1 Introduction..... | 5 |
| 2.2 Flow Governing Equations..... | 5 |
| 2.3 Flow Solution Method..... | 6 |
| 2.4 Burning Rate Calculations..... | 8 |
| | |
| 3 Structural and Fluid-Structure Considerations..... | 15 |
| 3.1 Introduction..... | 15 |
| 3.2 Mathematical Model..... | 15 |
| 3.3 Radial Natural Frequency Considerations..... | 19 |
| | |
| 4 Results and Discussion..... | 28 |
| 4.1 Introduction..... | 28 |
| 4.2 Results for Constant Cross-Section Reference Motors..... | 28 |

| | | |
|----------|---|-----------|
| 4.3 | Effect of Grain Area Transition Aspect Ratio..... | 37 |
| 4.4 | Effect of Grain Area Transition Position..... | 50 |
| 4.5 | Attenuation Maps..... | 54 |
| 4.6 | Effect of Transition Steepness..... | 60 |
| 5 | Conclusion..... | 65 |
| 5.1 | Final Remarks..... | 65 |
| 5.2 | Recommendations for Future Work..... | 65 |
| | References..... | 67 |

List of Tables

| | |
|---|----|
| Table 1-1: Reference Motor Characteristics..... | 4 |
| Table 3-1: Comparison of Radial Natural Frequency f_r For Different Approaches..... | 24 |
| Table 3-2: FE Radial Frequency Results for Different Propellant Inner Wall Radius Values of the Reference SRM..... | 25 |

List of Figures

Figure 1-1: Reference SRM and its grain port area expansion and contraction variants.... 3

Figure 2-1: Frequency response of reference propellant ($r_{b,o} = 1.27 \text{ cm/s}$, $K_b = 20000 \text{ s}^{-1}$, differing ΔH_s) in terms of nondimensional limit magnitude.....11

Figure 3-1: Plane Strain FE Model of the Reference SRM..... 21

Figure 3-2: Plane Strain Slice FE Model of the Reference SRM..... 22

Figure 3-3: 3D Solid Slice Model (version with 90 degree transition shown)..... 23

Figure 3-4: Lowest Radial Mode Corresponding to Model Depicted in Fig. 3-3.....24

Figure 3-5: Ring Mode Frequency of the Reference SRM as a Function of Propellant Inner Wall Radius..... 26

Figure 4-1: Predicted head-end pressure-time profile, reference motor – straight cylinder, 3.6 cm port diameter – acceleration effects nullified..... 29

Figure 4-2: Head end vs. Nozzle End Wave Profile – straight cylinder, 3.6 cm port diameter – acceleration effects nullified..... 30

Figure 4-3: Predicted head-end pressure-time profile, reference motor - straight cylinder, 3.6 cm port diameter – acceleration effects active..... 31

Figure 4-4: Head end vs. Nozzle End Wave Profile – straight cylinder, 3.6 cm port diameter – acceleration effect active.....32

Figure 4-5: Predicted head-end wave profile – straight cylinder, 3.6 cm port diameter – radial frequency held constant vs. variable- acceleration effect active.....33

Figure 4-6: Predicted head-end pressure-time profile, reference motor – straight cylinder, 5.09 cm port diameter – acceleration nullified.....34

Figure 4-7: Predicted head-end pressure-time profile – straight cylinder, 5.09 cm port diameter – acceleration effect active.....35

Figure 4-8: Predicted head-end pressure-time profile – straight cylinder, 5.09 cm port diameter – starting pressure 12.1 Mpa - acceleration effects active..... 36

Figure 4-9: Predicted head-end pressure-time profile – straight cylinder, 5.09 cm port diameter – starting pressure 7.95 Mpa - acceleration effects active..... 37

| | |
|--|----|
| Figure 4-10: Predicted head-end pressure-time profile – 1.25:1 contraction at grain position 0.4L – acceleration active..... | 38 |
| Figure 4-11: Predicted head-end pressure-time profile – 1.5:1 contraction at grain position 0.4L – acceleration active..... | 39 |
| Figure 4-12: Predicted head-end pressure-time profile – 2:1 contraction at grain position 0.4L – acceleration active..... | 40 |
| Figure 4-13: Predicted head-end pressure-time profile – 2.5:1 contraction at grain position 0.4L – acceleration active..... | 40 |
| Figure 4-14: Predicted head-end pressure-wave profile for grain port area contractions of various aspect ratios - grain position 0.4L – acceleration active..... | 41 |
| Figure 4-15: Predicted head-end pressure-time profile –1.5:1 expansion at grain position 0.4L – acceleration active..... | 42 |
| Figure 4-16: Comparison of head-end and nozzle-end pressure-wave profiles –1.5:1 expansion at grain position 0.4L – acceleration active..... | 42 |
| Figure 4-17: Predicted head-end pressure-time profile –1.75:1 expansion at grain position 0.4L – acceleration active..... | 43 |
| Figure 4-18: Comparison of head-end and nozzle-end pressure-wave profiles –1.75:1 expansion at grain position 0.4L – acceleration active..... | 44 |
| Figure 4-19: Predicted head-end pressure-time profile –2:1 expansion at grain position 0.4L – acceleration active..... | 44 |
| Figure 4-20: Predicted head-end pressure-time profile –2.5:1 expansion at grain position 0.4L – acceleration active..... | 45 |
| Figure 4-21: Predicted head-end pressure-wave profile for grain port area expansions of various aspect ratios - grain position 0.4L – acceleration active..... | 45 |
| Figure 4-22: Attenuation vs. Contraction aspect ratio - grain position 0.4L..... | 47 |
| Figure 4-23: Attenuation vs. Expansion aspect ratio - grain position 0.4L..... | 47 |
| Figure 4-24: Predicted motor-midpoint normal acceleration at the sleeve external surface -time profile –1.5:1 expansion at grain position 0.4L..... | 49 |
| Figure 4-25: Predicted motor-midpoint normal acceleration at the sleeve external surface -time profile –2:1 expansion at grain position 0.4L..... | 49 |

| | |
|--|----|
| Figure 4-26: Predicted head-end pressure-time profile –2:1 contraction at grain position 0.75L – acceleration active..... | 51 |
| Figure 4-27: Predicted head-end pressure-time profile –2:1 expansion at grain position 0.25 – acceleration active..... | 51 |
| Figure 4-28: Attenuation vs. axial position of transition – acceleration nullified..... | 53 |
| Figure 4-29: Attenuation vs. axial position of transition – acceleration active..... | 53 |
| Figure 4-30: Attenuation map: grain contraction, acceleration nullified, ref. time at $t = 0.26$ s, initial pressure disturbance of 2 atm, transition length of 0.156 m (36 cells, 30% of grain length)..... | 56 |
| Figure 4-31: Attenuation map: grain expansion, acceleration nullified, ref. time at $t = 0.26$ s, initial pressure disturbance of 2 atm, transition length of 0.156 m (36 cells, 30% of grain length)..... | 57 |
| Figure 4-32: Attenuation map: grain contraction, acceleration active, ref. time at $t = 0.26$ s, initial pressure disturbance of 2 atm, transition length of 0.156 m (36 cells, 30% of grain length)..... | 58 |
| Figure 4-33: Attenuation map: grain expansion, acceleration active, ref. time at $t = 0.26$ s, initial pressure disturbance of 2 atm, transition length of 0.156 m (36 cells, 30% of grain length)..... | 59 |
| Figure 4-34: Attenuation vs. transition length – 2:1 expansion - acceleration nullified..... | 60 |
| Figure 4-35: Attenuation vs. transition length – 2:1 expansion - acceleration active..... | 61 |
| Figure 4-36: Attenuation map: grain 2: 1 expansion, acceleration nullified, ref. time at $t = 0.26$ s, initial pressure disturbance of 2 atm..... | 63 |
| Figure 4-37: Attenuation map: grain 2: 1 expansion, acceleration active, ref. time at $t = 0.26$ s, initial pressure disturbance of 2 atm..... | 64 |

Nomenclature

| | |
|--------------|---|
| A | local core cross-sectional area, m^2 |
| A_d | downstream core cross-sectional area, m^2 |
| A_u | upstream core cross-sectional area, m^2 |
| a_t | longitudinal (or lateral) acceleration, m/s^2 |
| a_n | normal acceleration, m/s^2 |
| C | de St. Robert coefficient, $m/s\text{-Pa}^n$ |
| C_m | particle specific heat, $J/kg\text{-K}$ |
| C_p | gas specific heat, $J/kg\text{-K}$ |
| C_s | specific heat (solid phase), $J/kg\text{-K}$ |
| d | local core hydraulic diameter, m |
| E | local total specific energy of gas in core, J/kg |
| E_p | local total specific energy, particle phase in flow, J/kg |
| f | frequency, Hz, or Darcy-Weisbach friction factor |
| f_r | resonant combustion frequency, Hz |
| ΔH_s | net surface heat of reaction, J/kg |
| h | effective heat transfer coefficient under transpiration, $W/m^2\text{-K}$ |
| h_A | propellant web thickness, m |
| K_b | burn rate limiting coefficient, s^{-1} |
| K_δ | shear layer coefficient (m^{-1}) |
| k | gas thermal conductivity, $W/m\text{-K}$ |
| k_s | thermal conductivity (solid phase), $W/m\text{-K}$ |
| M_a | magnitude of attenuation |
| M_r | limit magnitude (cyclic input) |
| m_p | mean mass of a particle, kg |
| n | exponent (de St. Robert's law) |
| p | local gas static pressure, Pa |
| Δp_d | initial pulse disturbance step pressure, Pa |
| Δp_w | limit pressure wave magnitude, peak-to-trough, Pa |
| Pr | Prandtl number |
| R | specific gas constant, $J/kg\text{-K}$ |
| Re_d | Reynolds number |
| r_b | instantaneous burning rate, m/s |
| $r_{b,o}$ | reference burning rate, m/s |
| $r_{b,qs}$ | quasi-steady burning rate, m/s |
| r_b^* | unconstrained burning rate, m/s |
| r_o | base burning rate, m/s |
| r_p | pressure dependent burning rate, m/s |
| r_u | velocity dependent burning rate component (erosive burning), m/s |
| r_a | acceleration dependent burning rate component, m/s |
| T_f | flame temperature, gas phase, K |
| T_i | initial temperature (solid phase), K |
| T_s | burning surface temperature, K |
| Δt | time increment, s |
| u | core axial gas velocity, m/s |

| | |
|-----------------|--|
| u_p | core axial particle velocity, m/s |
| v_f | nominal flamefront velocity, m/s |
| x | distance from head end, m |
| Δx | spatial increment in axial direction, m |
| y | radial distance from burning surface, m |
| Δy | spatial increment in radial direction, solid phase, m |
| Δy_{Fo} | Fourier limit spatial increment, m |
| α_p | particle mass fraction of overall core flow |
| α_s | thermal diffusivity (solid phase), m^2/s |
| δ_o | reference combustion zone thickness, m |
| δ_r | resultant combustion zone thickness, m |
| ε | propellant surface roughness, m |
| κ | vibration-based wall dilatation term ($1/A \cdot \partial A / \partial t$), s^{-1} |
| λ | axial displacement, m |
| ρ | gas density, kg/m^3 |
| ρ_p | density, particle phase in core flow, kg/m^3 |
| ρ_s | density (solid phase), kg/m^3 |
| ϕ | acceleration orientation angle, rad |
| ϕ_d | long./lateral-acceleration-based displacement orientation angle, rad |
| ω_{nR} | natural frequency of 1 st radial mode, rad/s |
| ω_{res} | damped resonant frequency, rad/s |
| ω_{nL} | natural axial frequency, rad/s |
| ξ_L | axial damping ratio |
| ξ_R | radial damping ratio |
| Ψ | local instantaneous displacement under static loading, m |
| ζ | random position |

1 Introduction

1.1 Background

Combustion instability is a major consideration in the design and analysis of rocket motors. Unlike the case of liquid propellant engines, where instability symptoms have gained a lot of attention over the years, partly due to many spectacular booster rocket failures in the 1950's and 60's, understanding and analysis of means for the suppression of combustion instability symptoms as pertains to solid rocket motors (SRMs) has progressed at a slower, albeit even pace. Two principal categories of combustion instability can be observed in SRMs: axial and transverse (tangential, radial) combustion instability, where the former occurs at significantly lower frequencies, and with both categories delivering potentially damaging effects. Axial instability behavior is characterized by a development of a sustained axial pressure wave traveling back and forth along the motor chamber, often accompanied by a significant rise in base chamber pressure, called a DC shift. For years, the most effective solution in the event of symptoms arising has been the addition of aluminum particles to the propellant, guided by empirical data or a "rule-of-thumb". In cases where utilization of aluminized propellant is not desirable or possible (or on occasion, adequately effective), a much more seldom used option exists: to modify the internal grain geometry.

Certain past applications have successfully used acoustic cavities or resonators, either embedded in, or positioned next to the propellant grain, as means of combustion instability (CI) suppression in SRMs.^{1,2} However, introducing propellant grain (the word "grain" refers here to the entire propellant body or charge) area transitions can also be a potentially very effective means of suppressing axial pressure wave related instabilities in SRMs. This method by analogy has proven to be very effective in more commonplace acoustic applications such as automotive intake and exhaust systems, where an "expansion chamber", which is in effect a flow area expansion followed by a contraction, can be found alongside other acoustic devices such as the previously noted Helmholtz resonator or the quarter-wave resonator.

Unlike their counterparts in automotive technology, which can be successfully analyzed using acoustic approaches, flow area transitions in solid rocket motors necessitate a more comprehensive approach for their analysis, largely because of the highly non-linear nature of the flow, and the interrelation between the flow, the combustion process, and the surrounding structure. Studies of nonlinear axial combustion instability have ranged from numerous experimental test firing series on the one hand³, and linear/nonlinear acoustic theory modeling on the other.^{4,5-7} On occasion, researchers have employed a numerical modeling approach, to work towards a more comprehensive quantitative understanding of the physics involved.⁸⁻⁹ A survey of the literature has shown a relatively small number of studies have been performed on the use of grain area transitions as a means of CI suppression in solid rocket motors. Experimental studies performed by Koreki et al.¹⁰, and later, by Golafshani et al.¹¹, have confirmed the potentially advantageous effect of left-to-right grain area transitions as a means to control or suppress combustion instability. In that research, convergent port configurations (higher port diameter at the motor head end, as compared to the nozzle end of the propellant grain) were found to be generally more effective in suppressing combustion instability symptoms than divergent port configurations. For further background, examples of past computational studies related to the topic can be found in references 12 and 13.

1.2 Objective

The objective of this work is to investigate the effectiveness of grain port area transitions in a solid rocket motor, examining their ability to suppress axial combustion instability behavior. Both grain port area expansions and contractions are evaluated for a reference cylindrical grain motor. Various transition parameters such as the aspect ratio (ratio of propellant port hydraulic diameters on either side of the transition), its position along the grain, and transition steepness are considered.

1.3 Approach and Computational Model

The computational approach follows that used by Greatrix and Harris¹⁴ in the analysis of a small, high length-to-diameter solid rocket motor of a relatively constant cross-section. This motor, which forms the reference case for the purpose of this study, was also analyzed by other researchers using a coupled fluid-finite element interaction approach for a sample

pulsed-firing simulation.^{15,16} Based on past experience, the computational approach relying on thick wall theory and incompressible material characterization was employed here, as per Greatrix and Harris¹⁴, with the pertinent natural radial frequency as a function of propellant web thickness being obtained from FEA. This approach offered good agreement and correlation to past computational and experimental data, while enabling a sufficient number of computational runs to take place, as to then allow the completion of pertinent parametric studies and various trend charts for the present investigation.

The basic parameters of the reference motor are listed in Table 1-1. Figure 1-1 shows a schematic of the reference motor, with a depiction of motors with a left-to-right grain port area expansion and contraction, developed upon that baseline configuration. A thick-walled static-test sleeve surrounds a thin-walled aluminum motor casing.

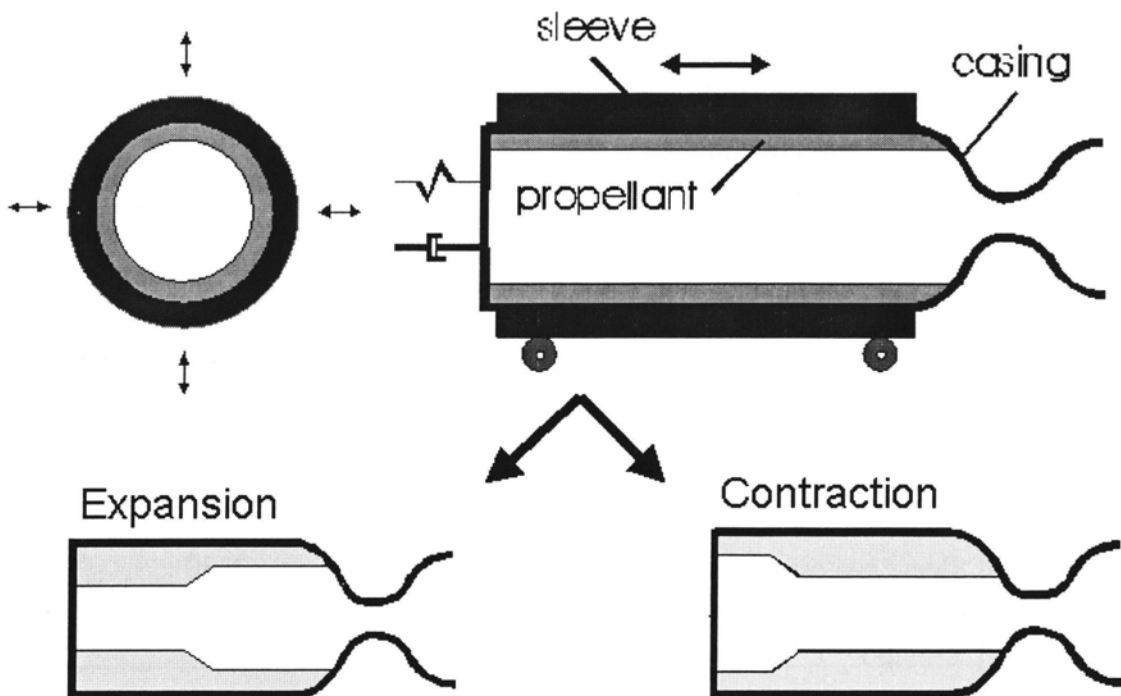


Figure 1-1: Reference SRM and its grain port area expansion and contraction variants

Table 1-1: Reference Motor Characteristics

| | |
|--|---|
| Propellant grain length, L_p | 52 cm |
| Initial port diameter, d_i | 3.6 cm |
| Nozzle throat diameter, d_t | 1.6 cm |
| Grain/nozzle-conv. length ratio, L_p/L_c | 16:1 |
| Propellant specific heat, C_s | 1500 J/kg-K |
| Propellant density, ρ_s | 1730 kg/m ³ |
| Propellant thermal conductivity, k_s | 0.4 W/m-K |
| Propellant thermal diffusivity, α_s | 1.54×10^{-7} m ² /s |
| Propellant flame temperature, T_f | 3000 K |
| Propellant surface temperature, T_s | 1000 K |
| Propellant initial temperature, T_i | 294 K |
| Gas specific heat, C_p | 1920 J/kg-K |
| Specific gas constant, R | 320 J/kg-K |
| Gas thermal conductivity, k | 0.2 W/m-K |
| Gas absolute viscosity, μ | 8.07×10^{-5} kg/m-s |
| Gas specific heat ratio, γ | 1.2 |
| De St. Robert exponent, n | 0.35 |
| De St. Robert coefficient, C | 0.05 cm/s-(kPa) ⁿ |
| Particle solid density, ρ_m | 2700 kg/m ³ |
| Particle specific heat, J/kg-K | 900 J/kg-K |
| Particle mass fraction, α_p | 0% |
| Propellant elastic modulus, E_A | 45 MPa |
| Propellant Poisson's ratio, ν_A | 0.497 |
| Casing inner wall radius, r_m | 3.24 cm |
| Casing wall thickness, h_B | 0.127 cm |
| Casing material density, ρ_B | 2700 kg/m ³ |
| Casing elastic modulus, E_B | 80 GPa |
| Casing material Poisson's ratio, ν_B | 0.33 |
| Sleeve wall thickness, h_C | 0.47 cm |
| Sleeve material density, ρ_C | 7850 kg/m ³ |
| Sleeve elastic modulus, E_C | 200 GPa |
| Sleeve material Poisson's ratio, ν_C | 0.30 |
| Casing/prop. rad. damping ratio, ξ_R | 0.35 |
| Casing/prop. long. damping ratio, ξ_L | 0.10 |

2 Fluid Dynamics and Combustion Considerations

2.1 Introduction

The underlying internal ballistic fundamentals of the computational model employed in this study are discussed in this section. The governing flow equations are discussed first, followed by a description of the flow solution method and details of the corresponding propellant burning rate calculations.

2.2 Flow Governing Equations

The relatively large length-to-diameter ratio of the motor under consideration allowed the usage of quasi-one-dimensional conservations equations for axial gas flow in this computational study. This however posed some limitations on the steepness of the motor core area change – to assure 2D and 3D effects remain insignificant. The applicable conservation equations for the gas flow, given below, are composed of homogenous terms on the left side, akin to those typically used for duct flows, and inhomogeneous terms on the right side, specific to SRMs or similar systems¹⁷.

$$\frac{\partial \rho}{\partial t} + \frac{\partial(\rho u)}{\partial x} = -\frac{1}{A} \frac{\partial A}{\partial x} \rho u + (1 - \alpha_p) \rho_s \frac{4r_b}{d} - \left(\frac{4r_b}{d} + \kappa\right) \rho \quad (1)$$

$$\frac{\partial(\rho u)}{\partial t} + \frac{\partial}{\partial x}(\rho u^2 + p) = -\frac{1}{A} \frac{\partial A}{\partial x} \rho u^2 - \left(\frac{4r_b}{d} + \kappa\right) \rho u - \rho a_\ell - \frac{\rho_p}{m_p} D \quad (2)$$

$$\begin{aligned} \frac{\partial(\rho E)}{\partial t} + \frac{\partial}{\partial x}(\rho u E + up) = & -\frac{1}{A} \frac{\partial A}{\partial x}(\rho u E + up) - \left(\frac{4r_b}{d} + \kappa\right) \rho E \\ & + (1 - \alpha_p) \rho_s \frac{4r_b}{d} \left(C_p T_f + \frac{v_f^2}{2}\right) - \rho u a_\ell - \frac{\rho_p}{m_p} (u_p D + Q) \end{aligned} \quad (3)$$

where the total specific energy was defined for an ideal gas as:

$$E = p / [(\gamma - 1)\rho] + u^2 / 2 \quad (4)$$

In the above equations, variable ρ denotes density, u the velocity, p the pressure, r_b is the instantaneous burning rate, while A is the cross-sectional area of motor core and d denotes the hydraulic port diameter of the cross-section. The term κ , represents a wall dilatation term due to the structural deformation of the vibrating body (i.e., effectively, port area change of the vibrating propellant, excluding surface regression), and is given by:

$$\kappa = \frac{1}{A} \cdot \frac{\partial A}{\partial t} \quad (5)$$

Longitudinal acceleration a_t is present in both the momentum and energy conservation equations in the form of a body force contribution, and is a function of both time and position along the propellant grain. Several variables in Equations (1) through (3) are specific to 2-phase (gas-particle) flow within an SRM, and are shown here for the sake of completeness. Since the present study deals only with single-phase flow, it is noted that the particle mass fraction α_p is zero, and all terms where particle drag D and heat transfer Q appear, do not apply to the present study.

The above equations of motion must be solved in conjunction with the local burning rate r_b of the solid propellant, and the corresponding geometric deformation of the propellant/casing/sleeve ensemble.

2.3 Flow Solution Method

The set of hyperbolic partial differential equations given in the previous subsection was solved using a higher order version of the Random Choice Method (RCM), as described by Gottlieb and Greatrix¹⁷. The RCM is an explicit finite volume scheme, often used to solve fluid dynamics problems characterized by the presence of strong flow property gradients, i.e., shock waves and similar discontinuities. A brief account of the methodology is included here for completeness; readers are encouraged to refer to the publications cited for more details.

The defining characteristics of the Random Choice Method is its use of pseudo-random sampling of flow properties at a given position within the wave profile, in contrast to flow-averaging across an element, typical of most other finite volume methods. At every time step

Δt , a random position ζ in-between two adjacent nodes is selected, for every adjacent node pair. Flow variables at the randomly selected “intermediate” position are then computed from the known values at the adjacent nodes, using the quasi-steady flow equations (Equations (1) through (3), but with all time derivatives set to zero). This implies that under transient flow conditions, the solution thus interpolated will result in a flow discontinuity at the intermediate position, resulting in a choked flow condition over the element. If this eventuality arises, the quasi-steady solution is replaced with either an isentropic compression or rarefaction wave of strength such that the flow is just sonic at the intermediate position.

As a subsequent step, a higher-order planar Riemann approach is used to solve for wave motion arising from the discontinuity, and the flow properties are determined for the midpoint position along each flow element, at the end of the first half time-step.

Next, the inhomogeneous source terms of Equations (1) through (3), including those due to the grain and nozzle transition and propellant mass influx, which tend to add substantial artificial noise to the solution, are incorporated into the planar wave solution, using a second-order accuracy method described by Ben-Artzi and Falcovitz¹⁸. The remaining source terms that do not appreciably affect solution noise, including terms due to axial acceleration and radial wall dilatation, are incorporated into the Riemann solution using the operator time-splitting technique. The time derivatives are calculated using a weak-wave Eulerian scheme, in order to simplify the procedure (isentropic wave calculations, as opposed to calculations involving non-isentropic shock waves). The flow parameters, inhomogeneous terms included, are matched through the weak waves from left to right, with a contact surface allowing the calculation of the time derivatives arising from the random position of the intermediate point ζ at which the values were evaluated. As ζ does not normally coincide with the element midpoint, the influence of time derivatives within the inhomogeneous terms occurs over a shorter time span (Δt_{eff}) than the full half time step Δt . Consequently, the wave-corrected flow properties are found from:

$$\lambda^* = \lambda_0^* + \Delta t_{eff} \left(\frac{\partial \lambda}{\partial t} \right)_0 \quad (6)$$

where λ is the uncorrected flow property, λ^* is the wave-corrected value of the flow property, and λ_0^* is the solution to the Riemann problem at the midpoint. The wave-corrected flow property values obtained in this manner are then modified for the quasi-steady flow changes from the random intermediate position to the mid-node position, as done initially. This somewhat lengthy process solves for the corrected flow properties at the mid-node positions, concluding the first half-time step.

The same process is followed for the second half time step, except that the inputs are the flow properties at the mid-node positions (generated in the first half time step) and these are “repositioned” to the original nodal locations in a manner analogous to the described previously. The associated burning rate and structural radial dynamics equations are run twice, once for each half time step, to keep the fluid dynamics, the propellant regression rate and the vibration calculations running in unison.

2.4 Burning Rate Calculations

The transient, frequency-dependent propellant burning rate model used in the present simulation was based on the Zel’dovich-Novozhilov (Z-N) nonlinear method.^{19,20} The Z-N method is a phenomenological approach that relies on empirical steady-state burning information, in lieu of computed chemical kinetics. In this approach, the unsteady solid phase heat conduction equation is solved to obtain the instantaneous total burning rate at a given location on the propellant burning surface. The resulting instantaneous burning rate is also dependent on the quasi-steady burning rate (pressure, velocity and acceleration-dependent terms), as well as the temperature profile across the pertinent propellant solid-phase cross-section (heat penetration zone beneath the propellant surface). The Z-N relationship is typically found in the literature in its time-dependent temperature-based form:

$$T_{i,eff} = T_i - \frac{1}{r_b^*} \frac{\partial}{\partial t} \int_{-\infty}^0 \Delta T dy \quad (7)$$

where T_i is the initial propellant temperature, $\Delta T = T(y,t) - T_i$ is the temperature distribution in moving from the burning propellant surface at $y = 0$ (and $T = T_s$) to the location in the propellant cross-section where the temperature reaches T_i , and r_b^* is the total instantaneous burning rate. For the purpose of the present study, a modified equation based on Equation (7) was used, relating the burning rate to the temperature profile, as derived by Greatrix²⁰:

$$r_b^* = r_{b,qs} - \frac{1}{(T_s - T_i - \Delta H_s / C_s)} \frac{\partial}{\partial t} \int_{-\infty}^0 \Delta T dy \quad (8)$$

where $r_{b,qs}$ is the quasi-steady burning rate, ΔH_s is the net surface heat release and C_s is the specific heat of the solid phase.

From Equation (8) the nominal (unconstrained) instantaneous burning rate was obtained, its value at a given propellant grain location being solved at each time increment via numerical integration of the temperature distribution through the heat penetration zone of the solid phase. A fourth-order Runge-Kutta finite difference scheme was employed for calculating the transient heat conduction in the solid phase over each time step²⁰. A time step Δt of approximately 1×10^{-7} seconds was utilized, based on experience with similar prior motor simulations and associated flow calculation requirements (Courant-Friedrichs-Lewy [CFL] criterion). The corresponding spatial step Δy in the solid phase was set as per the Fourier stability requirement limit:

$$\Delta y_{Fo} = (2\alpha_s \Delta t)^{1/2} \quad (9)$$

where α_s is the thermal diffusivity of the solid phase. This time increment was coordinated between the flow and structural model solution systems to assure the different aspects of the computation process proceed in unison. Further details of the finite differencing scheme can be found in the references cited.^{20,21,22}

In the present study, the true instantaneous burning rate r_b was found as a function of r_b^* (unconstrained burning rate) through the empirical rate limiting equation,

$$\frac{dr_b}{dt} = K_b(r_b^* - r_b) \quad (10)$$

where the rate limiting coefficient K_b acts to effectively damp the unconstrained burning rate r_b^* , when for a finite time increment Δt :

$$K_b < \frac{1}{\Delta t} \quad (11)$$

Using this semi-empirical approach, the propellant frequency-dependent behavior was controlled by setting the propellant's resonant frequency f_r , via the value of K_b (20000 s^{-1}), to be on the order of 1 kHz (a typical value that might be expected for this type of composite propellant at the base burning rate encountered in this study). It is noted the value of f_r used herein is relatively close to the fundamental longitudinal acoustic frequency f_{1L} of the combustion chamber. Thus, the propellant frequency-dependence characteristics used in this study are close to the worst-case scenario in terms of susceptibility to axial combustion instability symptoms.

While the parameter K_b controls the resonant frequency of the propellant frequency-dependent combustion response, the severity of the response, its peak non-dimensionalized magnitude, is controlled by the propellant net surface heat release, ΔH_s . The predicted frequency response for the AP/HTPB (ammonium perchlorate/hydroxyl-terminated polybutadiene) propellant employed for this study, at three different settings for the net surface heat release values, were previously investigated by Greatrix²³ and may be viewed in Figure 2-1 (positive value, exothermic heat release). The general response is given in terms of the nondimensional limit magnitude M_r , as defined by

$$M_\ell = \frac{r_{b,peak} - r_{b,o}}{r_{b,qs,peak} - r_{b,o}} \quad (12)$$

where the reference burning rate $r_{b,o}$ in this case is the motor's approximate mean burn rate at the point of pulsing.

In the present study, the computations were run using a propellant frequency-dependent combustion response profile having a net surface heat release of 150000 J/kg, corresponding to a propellant having a significant susceptibility to instability symptoms, as a close-to-worst case scenario.

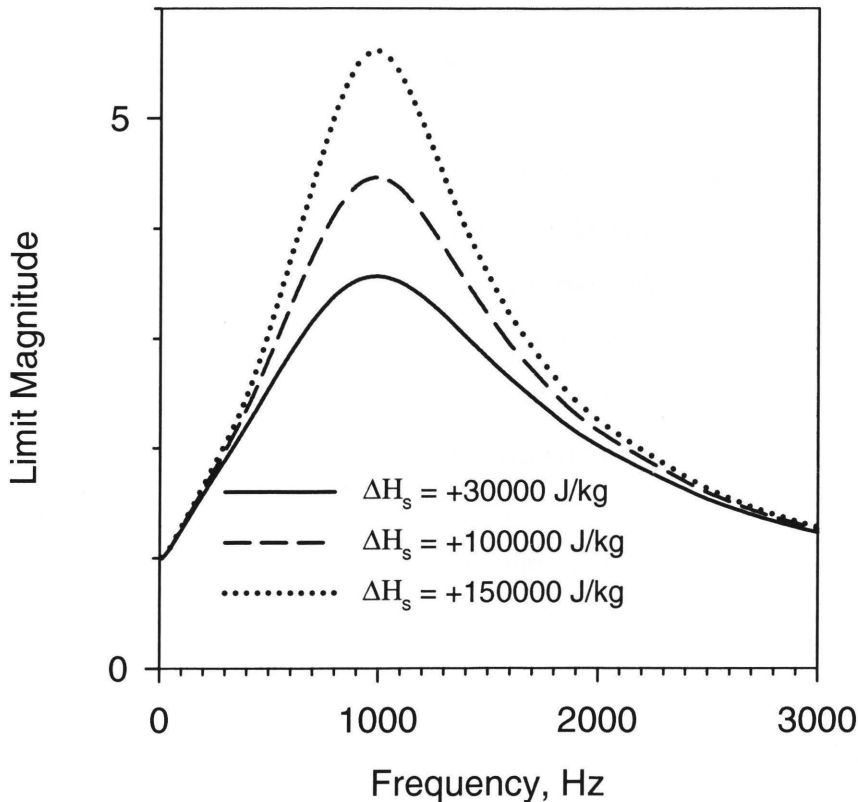


Figure 2-1: Frequency response of reference propellant ($r_{b,o} = 1.27$ cm/s, $K_b = 20000$ s⁻¹, differing ΔH_s) in terms of nondimensional limit magnitude

The quasi-steady burning rate $r_{b,qs}$, appearing in Equation (8), is the sum of pressure-dependent, velocity-dependent, and acceleration-dependent burning rate components. These are discussed in more detail below:

$$r_{b,qs} = r_p + r_u + r_a \quad (13)$$

The pressure-based burning component is determined from the well-known law of de St. Robert:

$$r_p = Cp^n \quad (14)$$

where n is the pressure exponent, p is the local static pressure, and C is the burning rate coefficient. The latter is a function of the bulk temperature of a given propellant and is given by:

$$C = C_0 \exp(\sigma_p(T_i - T_{io})) \quad (15)$$

where σ_p is the pressure-dependent burning rate temperature sensitivity (a property of a given propellant), and T_i is the initial temperature of the propellant. Parameters C_0 and T_{io} are respectively, the reference burning rate coefficient and the corresponding reference temperature. The inherent propellant parameters n , C_0 and σ_p are experimentally derived, typically using a strand burner or from a small-scale motor test. They can also be found in the open literature, for most commonly used solid propellants.

The velocity-dependent burning rate augmentation r_u , often called erosive burning, is determined via iterative means using Equations (16) through (20):

$$r_b = \frac{r_b}{r_o} \Big|_{\delta_r} \cdot r_o + r_u \quad (16)$$

where at lower flow speeds, the negative component resulting from a stretched combustion zone thickness δ_r , ($\delta_r > \delta_o$) may cause an appreciable drop in the base burn rate r_o , while at higher flow speeds, the positive erosive burning component r_u , established from a convective

heat feedback premise, dominates. The model used to relate r_u to other internal ballistic parameters is the Greatrix equation given by²⁴:

$$r_u = \frac{h(T_f - T_s)}{\rho_s [C_s(T_s - T_i) - \Delta H_s]} \quad (17)$$

where T_f is the temperature, T_s is the propellant surface temperature, C_s is the specific heat capacity of the propellant used, and ΔH_s , as before, is the surface heat of reaction. The convective heat transfer coefficient h , is defined as:²⁴

$$h = \frac{\rho_s r_b C_p}{\exp\left(\frac{\rho_s r_b C_p}{h^*}\right) - 1} \quad (18)$$

with:

$$h^* = \frac{k}{d} \text{Re}_d \text{Pr}^{1/3} \frac{f}{8} \quad (19)$$

where k is the thermal conductivity of the gas, and d is the hydraulic port diameter. Parameters Re_d and Pr are the familiar Reynolds number (in this case, Re is based on port diameter d) and the Prandtl number, while f is the Darcy-Weisbach friction factor, given by Colebrook's equation, valid for turbulent flow conditions:

$$f^{-1/2} = -2 \log_{10} \left(\frac{2.51}{\sqrt{f} \text{Re}_d} - \frac{\varepsilon/d}{3.7} \right) \quad (20)$$

with ε being the surface roughness of the propellant.

Acceleration-driven effects on the burning rate, crucial to this thesis, are based on a model combining normal, lateral, and longitudinal acceleration effects. The effects of acceleration normal to the burning surface a_n resulting from radial propellant/casing/sleeve vibration were included via the following equation:²⁵

$$r_b = \left[\frac{C_p (T_f - T_s)}{C_s (T_s - T_i) - \Delta H_s} \right] \frac{(r_b + G_a / \rho_s)}{\exp[C_p \delta_o (\rho_s r_b + G_a) / k] - 1} \quad (21)$$

In the above expression, the compressive effect of normal acceleration and the effect of steady or oscillatory longitudinal acceleration a_l was included through the accelerative mass flux G_a :

$$G_a = \left\{ \frac{a_n P}{r_b} \frac{\delta_o}{RT_f} \frac{r_o}{r_b} \right\}_{\phi=0^\circ} \cos^2 \phi_d \quad (22)$$

The reference film thickness δ_o is given by²⁵:

$$\delta_o = \frac{k}{\rho_s r_o C_p} \ln \left(1 + \frac{C_p (T_f - T_s)}{C_s (T_s - T_i) - \Delta H_s} \right) \quad (23)$$

and the displacement angle ϕ_d depends on the ratio of longitudinal to normal acceleration magnitudes:

$$\phi_d = \tan^{-1} \left[K \left(\frac{r_o}{r_b} \right)^3 \tan \phi \right] \quad (24)$$

It is noted that the longitudinal/lateral-acceleration-based displacement orientation angle ϕ_d is greater than the nominal acceleration vector orientation angle ($\phi = \tan^{-1}(a_l/a_n)$; or zero when only normal acceleration a_n relative to the burning propellant surface is present).²⁵ The normal acceleration vector appearing in the above equations is defined as being negative when acting to compress the combustion zone, but is set equal to zero when directed away from the zone (acceleration directed away from the propellant burning surface has no effect on the local burning rate). A typical value for the correction factor K is 8, based on comparisons to experimental data.

3 Structural and Fluid-Structure Considerations

3.1 Introduction

The structural model utilized in this study is based on the thick-walled cylinder approach, allowing for near-incompressible behavior of the propellant¹⁴. A mathematical model is given first, followed by a discussion of FEA-derived natural radial frequency. The structural vibrations of the propellant grain are excited by the back-and-forth passage of the axial pressure wave. The resulting acceleration of the propellant inner surface affects in turn the burning rate, as discussed in Section 2.4.

3.2 Mathematical Model

The analytical model employed follows a thick-wall theory approach used in a study by Greatrix and Harris¹⁴, except for a different treatment of the radial natural frequency ω_{nR} , allowing for its variation as a function of time and position along the grain in the present study. The aforementioned earlier study found that consideration of only the radial vibration of the independent ring elements provides for a reasonable agreement with the experimental data, for cylindrical grains.

The radial deformation dynamics of the propellant/casing/sleeve ensemble were considered separately at each station along the motor length (i.e., modeled using independent ring elements). The following ordinary differential equation applies for the movement of a radial position r within the assembly:

$$\frac{d^2 r}{dt^2} + (2\xi_R \omega_{nR}) \frac{dr}{dt} + \omega_{nR}^2 (r - r_0 - \psi) = 0 \quad (25)$$

In the above equation, r_0 is the reference radius when chamber pressure is zero, and ψ is the local instantaneous radial displacement under static loading. The radial damping ratio ξ_R was introduced to account for viscoelastic behavior of the propellant. This parameter is difficult to measure for an operating solid rocket motor, so a value of ξ_R of 0.35 based on previous studies performed on the same propellant and geometry, was used as being the most

appropriate. It is noted the damping effects can in general vary over the course of the firing, being the highest at the beginning of the run, when the propellant web thickness is at its maximum. However, variation of damping during the course of operation of the solid rocket motor was not investigated in the present work.

The fundamental natural radial frequency of the sleeve/casing/propellant assembly ω_{nR} , appearing in Equation (25) was determined using a commercial finite element analysis package, Nastran for Windows N4W. A more thorough discussion of this parameter, including its variation with time and propellant web thickness, is contained in the subsequent section of this report. The corresponding damped resonant frequency was ascertained via:

$$\omega_{res} = \omega_{nR} (1 - \zeta_R^2)^{1/2} \quad (26)$$

The local radial displacement under static loading was evaluated using the an ordinary differential equation based on thick-walled cylinder approach, given below:²⁶

$$\frac{d^2\psi}{dr^2} + \frac{1}{r} \frac{d\psi}{dr} - \frac{\psi}{r^2} = 0 \quad (27)$$

The solution of the equation (27) at the inner surface of the propellant ($r = r_i$) is:

$$\psi_i = A_1^A r_i + A_2^A / r_i \quad (28)$$

while at the exterior surface of the sleeve ($r = r_e$) it is:

$$\psi_e = A_1^C r_e + A_2^C / r_e \quad (29)$$

The coefficients A_1 and A_2 for their respective materials ($A =$ propellant, $B =$ aluminum casing, $C =$ steel sleeve) were obtained from the boundary conditions under static loading. At the inner propellant surface, under the local gauge static pressure $p(x)$, the applicable boundary condition is:

$$-p(x) = \frac{E_A}{(1+\nu_A)(1-2\nu_A)} \left[A_1^A - (1-2\nu_A) \frac{A_2^A}{r_i^2} \right] \quad (30)$$

where ν_A is the Poisson ratio of the propellant. At the same time, the corresponding boundary condition at the external surface of the sleeve (this surface is unloaded, so the LHS of Equation (31) is set to zero) is:

$$0 = \frac{E_C}{(1+\nu_C)(1-2\nu_C)} \left[A_1^C - (1-2\nu_C) \frac{A_2^C}{r_e^2} \right] \quad (31)$$

In addition to the outer boundary condition, compatibility conditions are implemented for each juncture (between propellant and casing, and between casing and sleeve) by setting the stress and displacement to be equal on both sides of each juncture. The coefficients (A's) are then solved for.

Longitudinal vibration was modeled as allowing the motor to move back and forth in the axial direction (nonrigid vibration, attached to a spring/damper load-cell representation). The following partial differential equation is used to describe the local axial displacement λ :¹⁴

$$\frac{\partial^2 \lambda}{\partial t^2} + 2\omega_{nL}\xi_L \left(\frac{\partial \lambda}{\partial t} - V_\infty \right) = \frac{E_B}{(1-\nu_B^2)} \frac{\Delta x}{\Delta m} \left[\frac{E_C(1-\nu_B^2)}{E_B(1-\nu_C^2)} A_C + A_B \right] \frac{\partial^2 \lambda}{\partial x^2} \quad (32)$$

The propellant was assumed to carry no load in the axial direction, due to its low modulus of elasticity (in comparison to the sleeve and the casing). However, the mass of the propellant for a given incremental distance Δx was included along with the casing, sleeve, retaining rod, and any attachment masses as part of Δm . The cross-sectional areas of the load bearing components are given by A_B (aluminum casing) and A_C (steel sleeve and retaining rods). If the pertinent axial damping ratio ξ_L is internal to the system, then the rigid-body reference velocity V_∞ must be included as shown (otherwise, if the damping is external damping, V_∞

would be set to zero in Equation (32)). The fundamental natural axial frequency ω_{nL} is approximated by:¹⁴

$$\omega_{nL} = \frac{\pi}{l_c} \left[\frac{\left(\frac{E_C(1-v_B^2)}{E_B(1-v_C^2)} A_C + A_B \right) E_B l_c}{m(1-v_B^2)} \right]^{1/2} \quad (33)$$

where l_c is the effective chamber length, and m is the overall uniformly distributed mass of the system. Equation (33) was solved via an explicit finite difference technique, with a numerical stability requirement on the time-step:²⁷

$$\Delta t \leq \left[\frac{(1-v_B^2) \Delta m \cdot \Delta x}{E_B \left(\frac{E_C(1-v_B^2)}{E_B(1-v_C^2)} A_C + A_B \right)} \right]^{1/2} \quad (34)$$

The boundary condition at the head-end of the motor is:

$$\frac{\partial \lambda}{\partial x} = \frac{-F_{he}(1-v_B^2)}{E_B \left(\frac{E_C(1-v_B^2)}{E_B(1-v_C^2)} A_C + A_B \right)} \quad (35)$$

While the boundary condition at the nozzle-end of the motor is ascertained via:

$$\frac{\partial \lambda}{\partial x} = \frac{F_{ne}(1-v_B^2)}{E_B \left(\frac{E_C(1-v_B^2)}{E_B(1-v_C^2)} A_C + A_B \right)} \quad (36)$$

The head-end force F_{he} , appearing in Equation (35), is determined via:

$$F_{he} = -p_{he} A_{he} + k(\lambda_1 - \lambda) + c \left(\frac{\partial \lambda_1}{\partial t} - \frac{\partial \lambda}{\partial t} \right) + D \quad (37)$$

where the variables p_{he} , A_{he} , k , c , and D respectively denote head-end pressure, head-end internal cross-sectional area, load-cell spring constant, load-cell damping constant, and external aerodynamic drag force (essentially zero for the test-stand case). The axial displacement λ_1 refers to the adjoining end-wall ($\lambda_1 = 0$) or to a movable mass ($\lambda_1 \neq 0$) to the left of the head-end of the motor.

The nozzle-end force, appearing in Equation (36) was determined via:

$$F_{ne} = -T + \int_{A_r}^{A_p} p dA \quad (38)$$

where T is the thrust generated from the nozzle, and the integral represents the instantaneous pressure force acting on the nozzle convergence (from grain port to nozzle throat).

3.3 Radial Natural Frequency Considerations

The usage of the independent ring element approach to model the structural dynamics of the solid rocket motor, and in particular, employment of the thick-wall approach as per Equation (25) of the previous section, requires unique values for the radial natural frequency ω_{nR} . Often called the “ring mode”, ω_{nR} corresponds to the physical deformation state of all parts of the cylindrical section undergoing uniform, purely radial (either inward or outward) displacement. In case of a thin ring, there is a single radial magnitude of displacement, and the corresponding frequency can be shown to be related to the speed of sound in the material:

$$f_r = \frac{C_L}{\pi d} \quad (39)$$

where C_L is the longitudinal wave speed in the material:

$$C_L = \sqrt{\frac{E}{\nu}} \quad (40)$$

The relation between the natural frequency as expressed in radians versus cycles is:

$$\omega_{nR} = 2\pi f_r \quad (41)$$

To account for the three different layers, a more complex equation could be used:

$$\omega_{nR} = \sqrt{\frac{\frac{E_A h_A}{r_A(1-\nu_A^2)} + \frac{E_B h_B}{r_B(1-\nu_B^2)} + \frac{E_C h_C}{r_C(1-\nu_C^2)}}{r_A h_A \rho_A + r_B h_B \rho_B + r_B h_B \rho_B}} \quad (42)$$

The above was shown in the study by Greatrix and Harris⁸ to offer a reasonable approximation to the experimentally measured radial frequency of vibration. However, a difference of over 20% was observed for the reference motor in the predicted frequency value given by the formula above in comparison to more detailed structural treatments relying on the use of finite elements as presented in Loncaric et al.¹⁵ and Montesano et al.¹⁶. To overcome that discrepancy, without resorting to a direct fluid structure interaction approach (which would have been computationally resource-prohibitive, given the nature of this study and the required number of simulation runs), the natural radial frequency was determined externally, using a commercial FE package (Nastran N4W), as a function of remaining propellant web thickness.

To that end, finite element models of the propellant/casing/sleeve ensemble were built in several variants, to ascertain the effect of mesh type and topology on the frequency corresponding to the ring mode. These variants included 2D plane strain element models: the entire cross section as well as just the slice (single element width), using 1st and then 2nd order elements, as well as a 3D (three-dimensional) “slice” model, employing 1st order elements only. These are briefly discussed in turn.

Figure 3-1 illustrates the basic 2D (two-dimensional) model, employing 1680 quadrilateral plane-strain elements (FE software utilized for this work has a built-in “plane strain” element

type). Material properties are as per Table 1-1. It is noted the plane strain assumption is exact for a cylinder of infinite length – in the case of a solid rocket motor, it is a close approximation for regions near the midsection of the motor, but is less exact near the ends, where a plane stress assumption would be more appropriate (however, the endcap effects might have a more significant impact in those regions, and this in turn depends on the motor construction details, e.g., whether the grain is partially or fully bonded at the ends, or whether it is free).

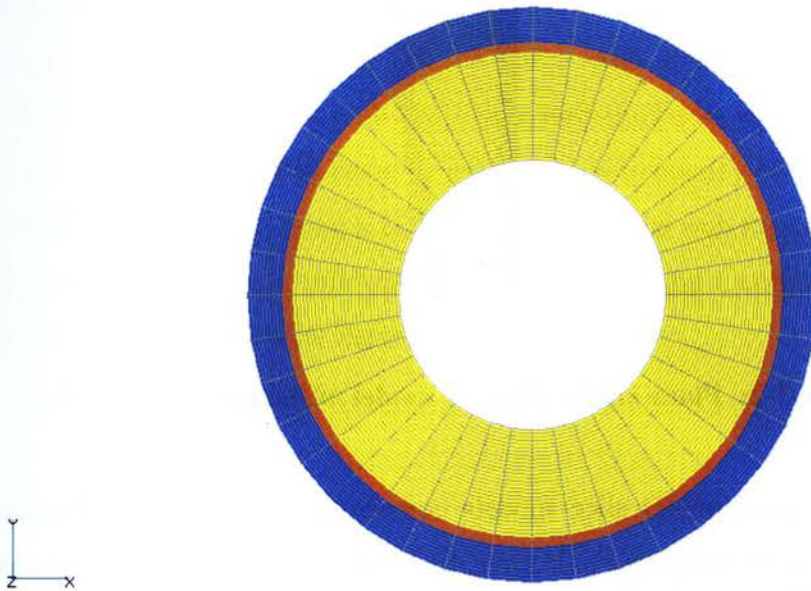


Figure 3-1: Plane strain FE model of the reference SRM

In order to capture radial modes only (frequency of the ring mode being investigated), the model was supported by constraining the tangential degree of freedom for each node – effectively disassembling the model into a collection of radial slices. Thus, for simplicity and computational efficiency, a slice model as shown in Figure 3-2 was employed. The results obtained for the whole cross-section and the slice model were, as expected, practically identical, with the difference being 1 Hz. Two variants of the slice model were used: the frequency obtained using the 1st order mesh (corner nodes only) was 14,303 Hz, while a 2nd

order mesh (corner and midside nodes, quadratic interpolating function) of the same topology resulted in a natural radial frequency of 14,335 Hz, a mere 0.2% difference.

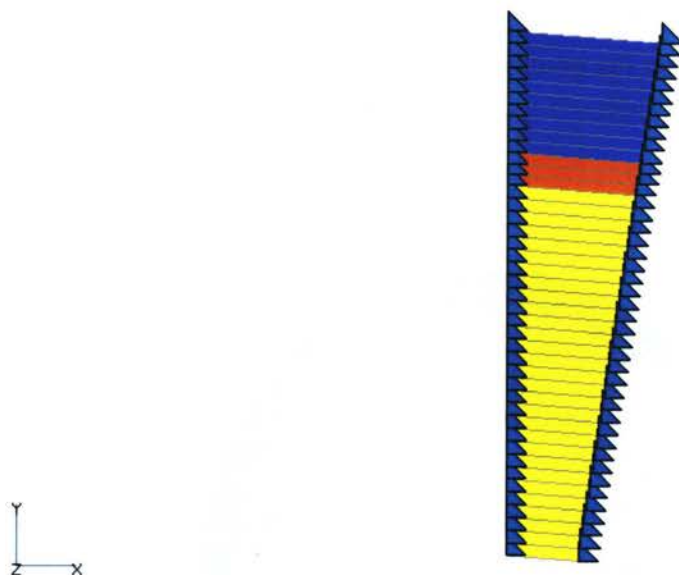


Figure 3-2: Plane strain slice FE model of the reference SRM

In addition, two variants of 3D slice models composed of 1st-order solid elements were investigated: one corresponding to a uniform cylindrical model (2730 elements) and the other comprising a step grain area transition (area transition ratio of 2:1, step positioned at 40% of the length, 2340 elements) as illustrated in Figure 3-3. Longitudinal and tangential degrees of freedom were constrained for all nodes, as only the symmetric radial modes were of interest. The natural frequency obtained for the model without the transition was 14,302 Hz, in near-exact agreement with the 2D plane strain model. The mode shape, in the absence of any additional end supports (i.e., the ends were modeled as being free) was that of a uniform radial extension throughout, with the greatest deformation magnitude obtained, as expected, at the inner wall of the propellant. The potential effect of the endcaps was also investigated. It was found the presence of such end constraints (if propellant is partially or fully bonded to the nozzle or the head end) had surprisingly little effect on the natural frequency (increase of less than 2% for the reference SRM), but of course, did have a significant impact on the

deformation. It is noted that in the case of fully bonded propellant ends, their displacement is limited to whatever value the much stiffer nozzle or casing material deforms to, while if the grain ends are free, the effects of the endcaps on the radial vibration frequency of the grain is only indirect, resulting from a reduced displacement of the casing or the sleeve.

The analysis performed on the 3D slice model with a grain area transition has not shown a single uniform-throughout mode shape. Instead, a collection of ring modes was found to exist, with the lowest one corresponding to maximum displacement amplitude occurring at the more compliant end (in effect, the end where the propellant web thickness is higher), with resonant frequency of 14,336 Hz – i.e., a 0.2% difference from the results found for the constant diameter SRM model of the same web thickness. Maximum displacement amplitude at the motor end with the lower web thickness (port area twice as high as the previous case) was found to occur at mode with a frequency of 20.2 KHz, which compares with 20.0 KHz predicted using a 2D model for the same web thickness. Thus, accounting for modal superposition, it is believed the approach of using a collection of ring elements is a reasonable approximation for the problem at hand.

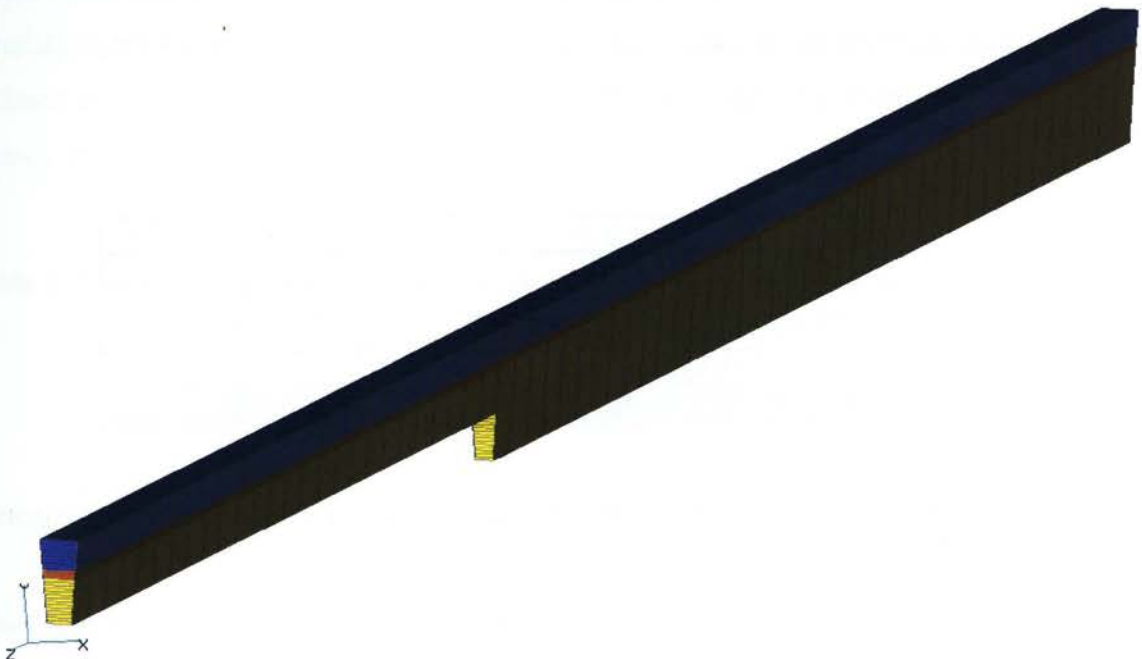


Figure 3-3: 3D solid slice model (version with 90 degree transition shown)

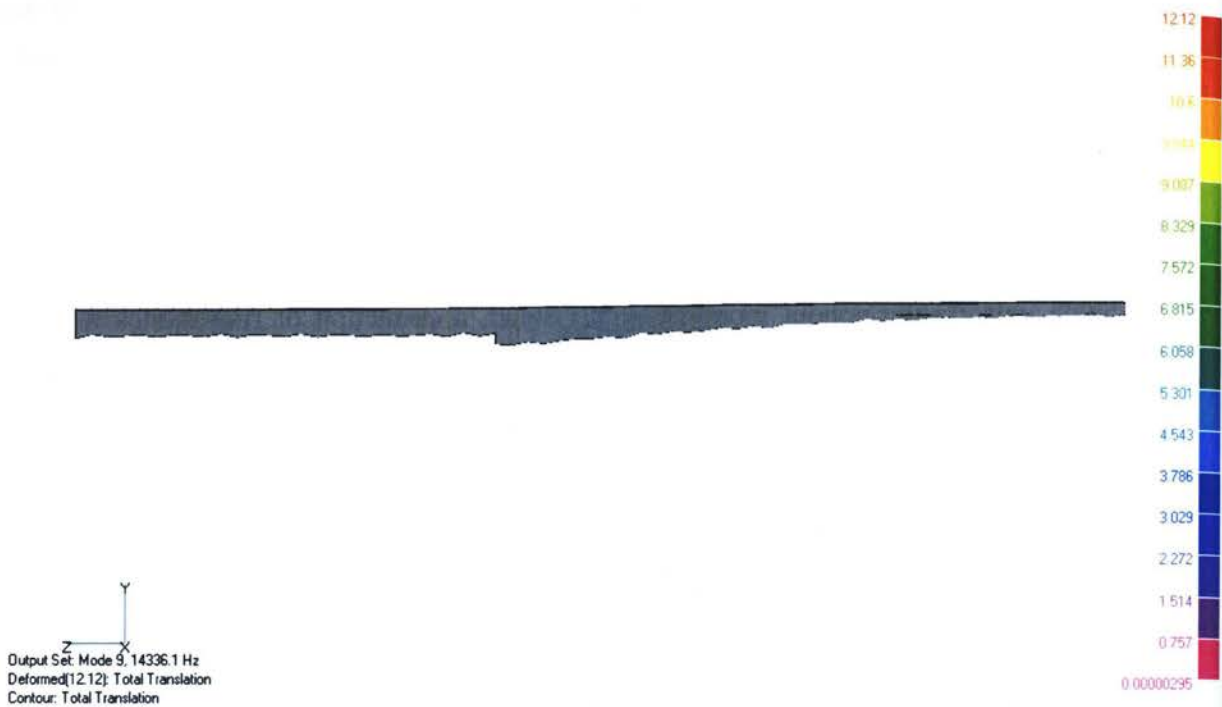


Figure 3-4: Lowest radial mode corresponding to model depicted in Fig. 3-3

A comparison of the first extensional radial mode undamped natural frequency obtained using the different models and Equation (42) is shown in Table 3-1, for the propellant web thickness at the beginning of the firing.

| Approach | Natural Frequency (Hz) |
|-----------------------------------|------------------------|
| Equation 41 | 19839 |
| 2D Slice model - 1st order | 14303 |
| 2D Slice model - 2nd order | 14335 |
| 3D Uniform cylinder slice | 14302 |
| 3D Cylinder slice with transition | 14336 |

Table 3-1: Comparison of Radial Natural Frequency f_R For Different Approaches

As can be seen, the results obtained using finite element models were consistent with each other – and all differed significantly from the analytical expression based on the thin-wall approach. This discrepancy was investigated further, by modifying the model of Figure 3-2, by removing the propellant elements, but adding the mass of the propellant to the casing

elements (i.e., as equivalent density of the casing material, which includes the mass of both casing and propellant, but only the casing stiffness). The resulting natural radial frequency of 19,829 Hz was almost identical to that obtained from Equation (42). It was concluded that the aforementioned equation overestimates the frequency as a result of not accounting for the motion of the very compliant propellant (it grossly oversimplifies the radial distribution of mass and stiffness). It was also observed that changing the web thickness, modulus of elasticity of the propellant, or its Poisson's ratio, shows virtually no effect on the frequency if Equation (42) is being used. In contrast, studies performed using the FEA approach did indicate a significant effect of each of the above three parameters. In particular, the effect of web thickness on the radial frequency was of interest to this study, as does the change in frequency during the burnback cycle.

To obtain a relationship between the propellant inner wall radius (which is progressively reduced during the burnback cycle) and the radial vibration frequency, 9 separate cases of the model depicted in Figure 3-2 were run; the first case was the reference SRM with the starting radius of 0.0180 m, with the previously determined frequency of 14,302 Hz. For each subsequent run, the propellant inner wall radius (and hence, web thickness, as the propellant outer wall radius stays unchanged) was reduced by successively deleting the elements (and associated nodes) from the interior of the model. Table 3-2 lists the results obtained for the reference SRM.

Table 3-2: FE Radial Frequency Results for Different Propellant Inner Wall Radius Values of the Reference SRM

| Propellant inner wall radius (m) | FE-predicted radial frequency (Hz) |
|----------------------------------|------------------------------------|
| 0.01800 | 14302 |
| 0.02098 | 16558 |
| 0.02148 | 17054 |
| 0.02346 | 18614 |
| 0.02446 | 19346 |
| 0.02545 | 20024 |
| 0.02644 | 20659 |
| 0.02843 | 21801 |
| 0.03041 | 22834 |

The results indicated a definite increase of f_r with decreasing propellant web thickness, with the values approaching the natural radial frequency of the casing/sleeve combination, as the propellant is burned back. This relationship is indicated in Figure 3-5.

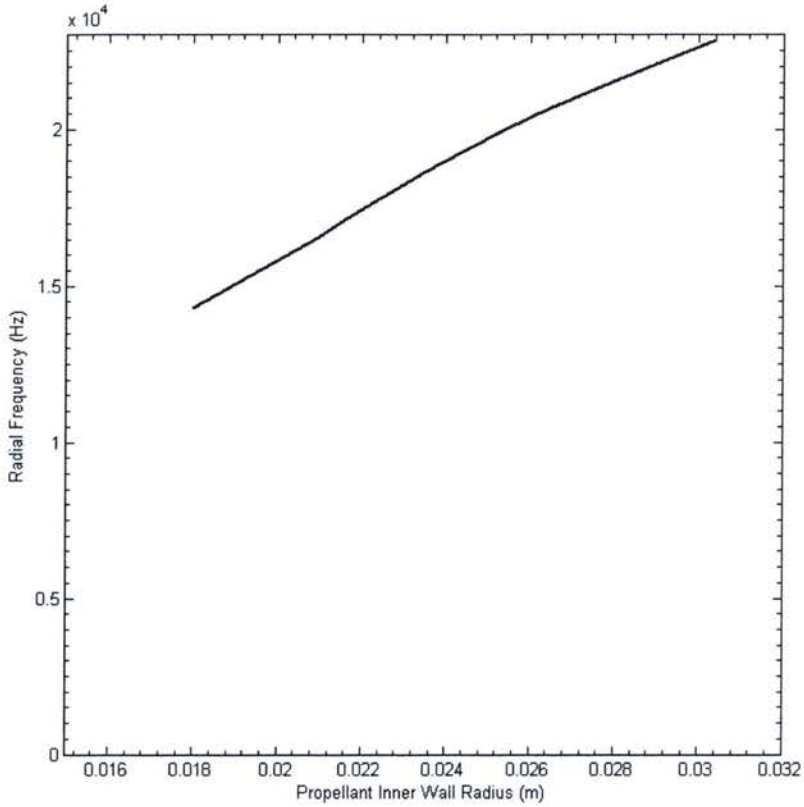


Figure 3-5: Ring mode frequency of the reference SRM as a function of propellant inner wall radius

In order to use the above results in the internal ballistic simulation, a cubic curve fit was used in MATLAB to obtaining the following expression between the f_r and the propellant inner wall radius for this reference SRM.

$$f_R \cong -1194000000r_i^3 + 71670000r_i^2 - 637800r_i + 9505 \quad (43)$$

MPa at the end of the simulation (reference value $t = 0.26$ sec). The 2-Atm pulse (introduced at $t = 0.0905$ sec) results in a much stronger sustained pressure wave in the chamber. The limit magnitude of that wave thereafter diminishes slowly with time, reaching 1.42 MPa at reference time of 0.26 seconds.

Figure 4-2 shows a comparison of the pressure wave profile for this case, as determined for the motor head end location (labeled H.E.) and the corresponding location at the end of the grain port, next to the nozzle (labeled N.E.). One can see the head end and the nozzle end profiles are exactly out of phase, as expected for a single traveling wave, and are nearly sinusoidal in shape. It is noted that although the peak pressure is the same for the head end and the nozzle end locations, the limiting wave magnitude is slightly higher for the nozzle end.

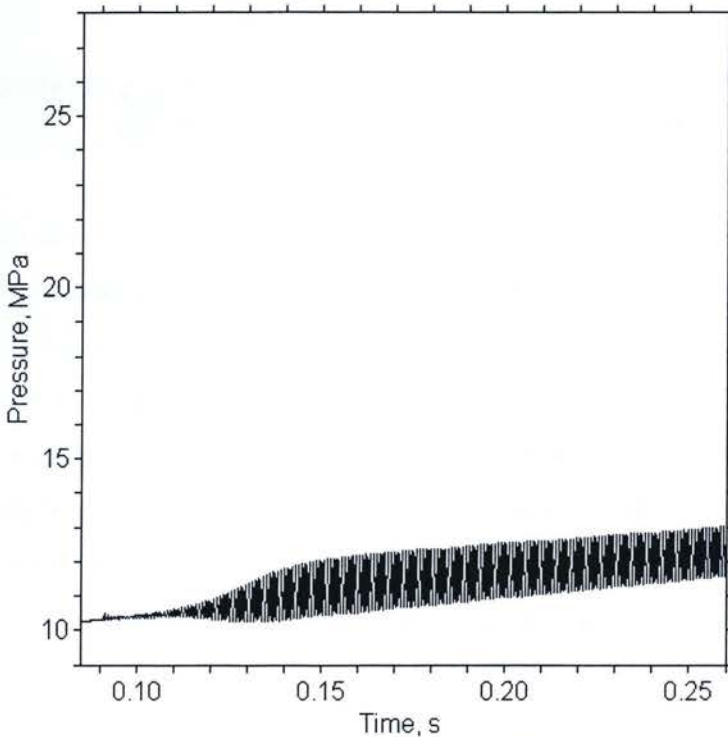


Figure 4-1: Predicted head-end pressure-time profile, reference motor – straight cylinder, 3.6 cm port diameter – acceleration effects nullified

4 Results and Discussion

4.1 Introduction

The results presented in the foregoing sections apply to the solid rocket motor with parameters as per Table 1-1, except that the internal port geometry is varied, to allow the implementation of grain area transitions.

All results pertain to the AP/HTPB propellant characteristics as per Section 3.4, with a K_b value of 20000 s^{-1} and a net surface heat release of 150000 J/kg , chosen to represent a propellant with an undesirable susceptibility to axial combustion instability symptoms.

Results for constant cross section “reference” cases are described first, followed by discussions of the effects of varying the area transition (either a left-to-right grain port area expansion or contraction) aspect ratio, position along the grain and steepness.

4.2 Results for Constant Cross-Section Reference Motors

As a prelude to the analysis of the reference SRM with grain area transitions, this subsection considers the results obtained for a straight-cylinder SRM geometry – with and without acceleration-based burning rate augmentation being included. The intent of this is threefold: to verify the correct working of the modified computational code, by comparing the results to prior similar results obtained by other investigators^{14,23}, to establish a baseline or a framework within which the results for the grain-area transition SRM can be interpreted, and to identify some basic trends which can later be used as a guide in assessing the effectiveness of the grain area transitions.

A study of the straight-cylinder reference SRM, with a starting port grain diameter of 3.6 cm was performed. Figure 4-1 depicts the profile of the head-end chamber pressure as a function of time. The results match exactly those obtained by Greatrix and Harris¹⁴, indicating the modifications to the code did not inadvertently affect its operation for non-accelerative cases. One can see during the course of the simulation the base pressure rises from its initial value of 10.0 MPa (at the end of the quasi-steady phase of the simulation) to approximately 11.5

of the DC shift in the simulations performed (see Sections 4.2 and 4.3 for more details). It was also noted that the presence of the nozzle appears to have a moderating effect on the peak of the shockwave.

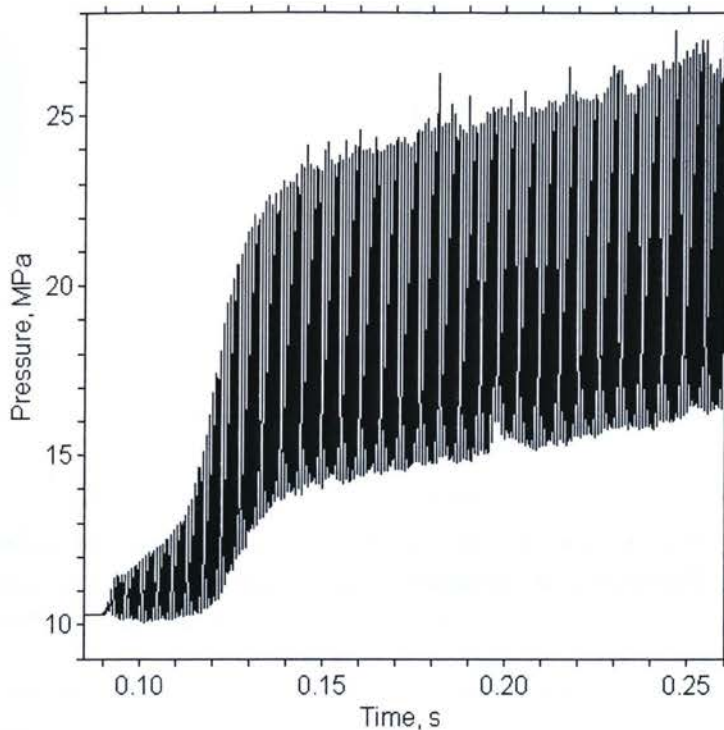


Figure 4-3: Predicted head-end pressure-time profile, reference motor – straight cylinder, 3.6 cm port diameter – acceleration effects active

As earlier studies did not consider the change in natural radial frequency during the burnback cycle (a mean value was employed), a comparison was made between the case represented by Figure 4-3, and the numerical analysis of the same motor performed by keeping the radial natural frequency constant at 15 kHz. For comparison, the variable-frequency formulation as per Section 3.3, employed throughout this study, corresponds to a shift in f_r from 14.3 kHz to about 18 kHz, as the cylindrical grain burns back from the initial port diameter of 3.6 cm, to a port diameter at the 0.26 sec reference time of about 4.5 cm.

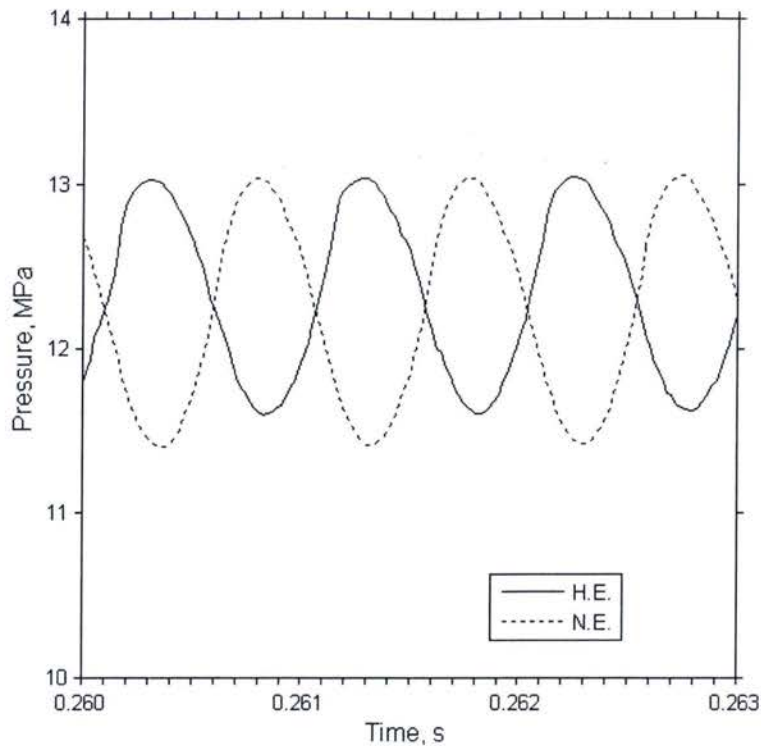


Figure 4-2: Head end vs. nozzle end wave profile – straight cylinder, 3.6 cm port diameter – acceleration effects nullified

The above evaluation was repeated, but this time with the effects of acceleration on the burning rate included in the simulation, as per Equation (21). The structural dynamics model described in Section 3.2 was employed, while the natural radial frequency was based on the analysis described in Section 3.3. The results show a significant rise in the base burning pressure (DC shift), coupled with a severe increase (by an order or magnitude) in the limit pressure wave magnitude – reaching 10.8 MPa at the reference time of 0.26 sec. It is clear that the motor described by Figure 4-3 is operating in a highly unstable, nonlinear regime. Once again, the results are in good agreement with those obtained earlier by Greatrix, where a limit pressure wave magnitude of 10.2 MPa was noted for the same SRM under relatively the same conditions.

Examining the head end and nozzle end pressure wave profiles corresponding to the above runs, one notes a very steep wavefront, indicative of a strong shockwave. Throughout this study, it was found that the presence of such shocks was linked to the coincident occurrence

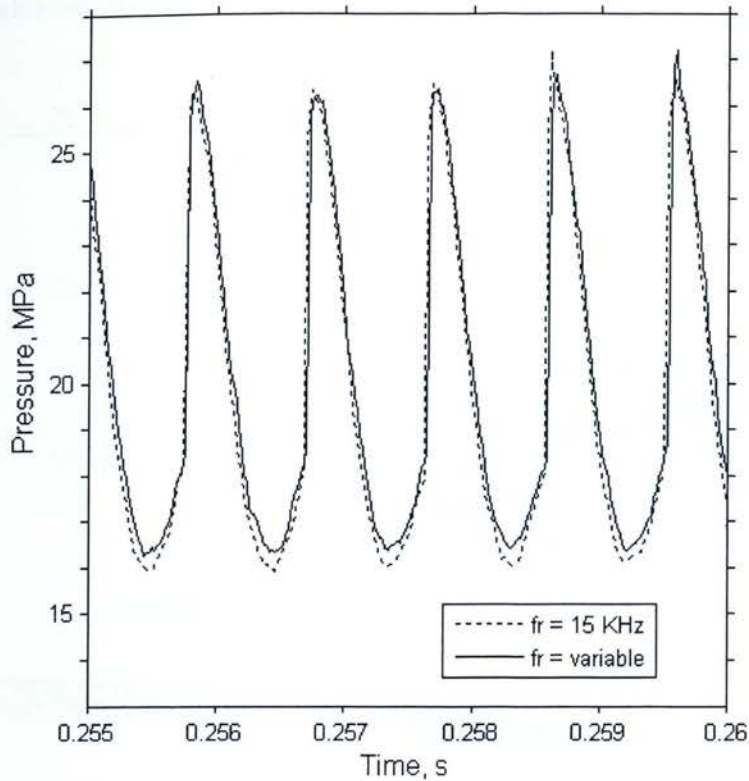


Figure 4-5: Predicted head-end wave profile – straight cylinder, 3.6 cm port diameter – radial frequency held constant vs. variable- acceleration effect active

While the above deliberations considered the reference SRM with a constant starting grain port diameter of 3.6 cm, additional computations were performed for an analogous straight cylinder motor with a port diameter of 5.09 cm, corresponding to a port area exactly twice that of the previous case. This was done to present a framework for the foregoing study of grain area transitions, by providing a sample “boundary case” (i.e., a reference SRM with a grain area transition of a 2:1 aspect ratio, would have a 3.6 cm port diameter on one side, and a 5.09 cm port diameter on the other).

As shown in Figure 4-6 for the acceleration-effects-nullified case, increasing the starting port diameter to 5.09 cm, results in a decrease in the limiting pressure wave magnitude to 1.18 MPa (vs. 1.42 MPa for d_p of 3.6 cm), for the same initial chamber pressure of approximately 10 MPa. Note that the nozzle throat area has been increased (from 1.60 cm to 1.86 cm) to provide a similar initial chamber pressure. While a larger port diameter would lower erosive burning for the same flow induced behind any traveling axial pressure waves, it is not clear

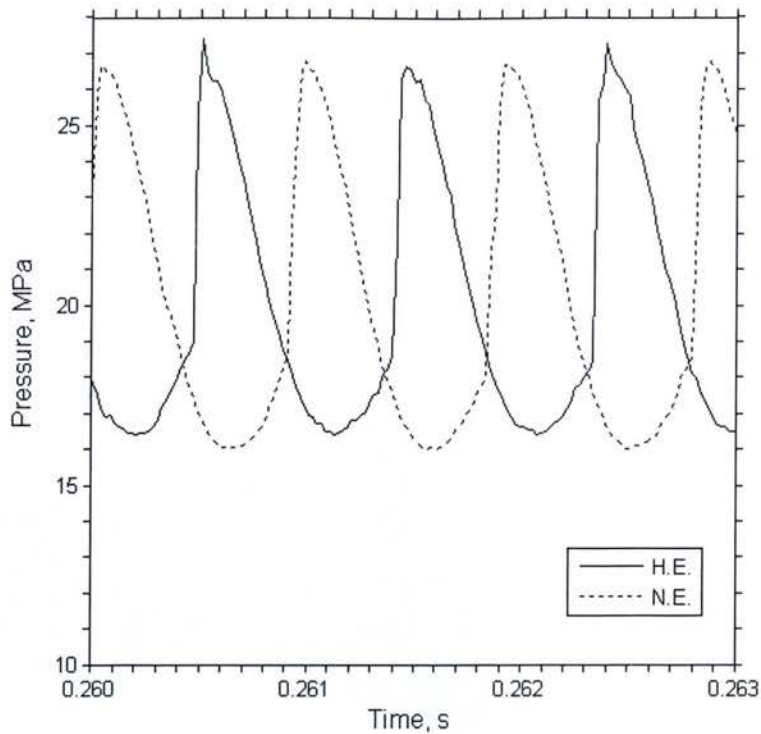


Figure 4-4: Head end vs. nozzle end wave profile – straight cylinder, 3.6 cm port diameter – acceleration effect active

As shown in Figure 4-5, the effect of the radial natural frequency on the limiting pressure wave magnitude and profile in the case of the straight-cylinder reference SRM was surprisingly small, given the dramatic effect the inclusion of the accelerative-based effects on the burning rate had on the same variables. This suggests the behavior observed in going from Figure 4-1 to Figure 4-3 is driven largely by the passage of the axial pressure wave inducing an instantaneous increase in the local burning rate, as opposed to resonant structural behavior of the propellant/casing/sleeve assembly. Of course, the latter would become much more important if the length of the chamber would be such as to place the frequency of the axial oscillations closer to the natural radial frequency. In this case, the oscillation frequency of the shock wave going back and forth through the chamber is 1050 Hz, which is well away from the radial natural frequency range of 14-18 kHz – hence, no resonant behavior can be observed.

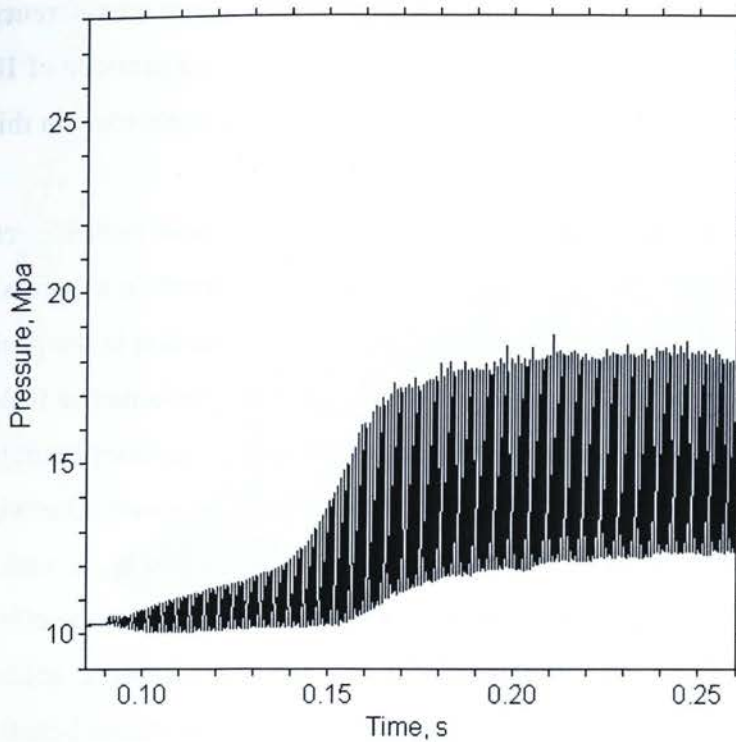


Figure 4-7: Predicted head-end pressure-time profile – straight cylinder, 5.09 cm port diameter – acceleration effect active

Finally, as a side study, the effect of varying the starting chamber pressure was verified, by changing the nozzle throat diameter, while keeping all the other parameters constant. Only two such cases were run, as this effect was only of ancillary interest, largely outside of the scope of the grain area transitions investigation presented in this thesis. The study was performed on the SRM of Figure 4-7, including the accelerative effects in the computations, for starting base pressures of about 8 MPa and 12 MPa. As evidenced by Figure 4-8, increasing the initial chamber pressure to 12 MPa, by decreasing the nozzle throat diameter while keeping all the other parameters constant, resulted in a drastic decrease in the limit pressure wave magnitude to about 1 MPa, as compared to 5.5 MPa for the case of Figure 4-7. A higher base pressure results in a higher base burning rate, which can significantly reduce burning augmentation due to Z-N transient response, flow velocity, and acceleration. This may explain to some degree the above result.

In contrast, changing the starting base pressure to 8 MPa, by increasing the nozzle throat diameter, resulted in a very rapid development of DC shift (see Figure 4-9). However,

that the induced flow speeds would be of sufficient strength to completely account for this difference in the limit pressure wave magnitudes.

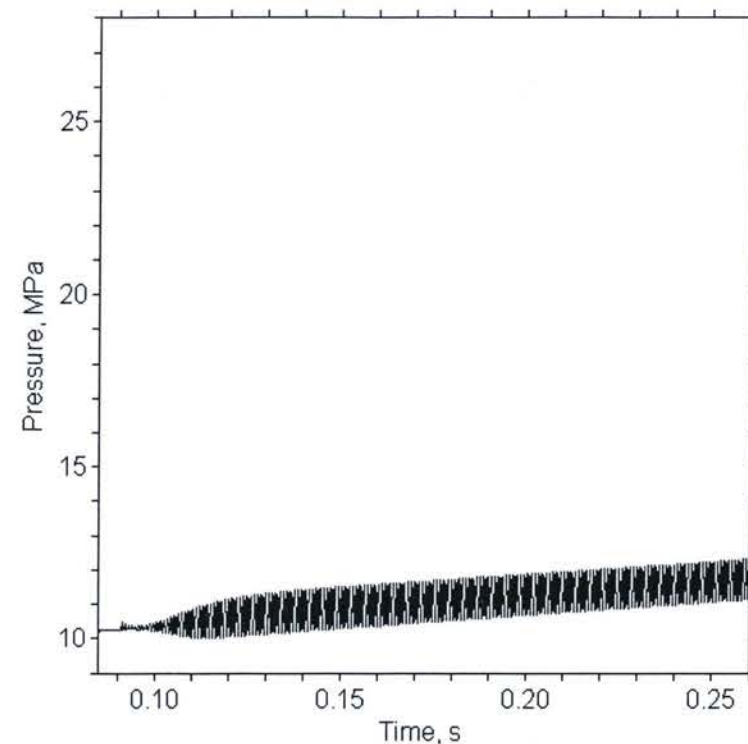


Figure 4-6: Predicted head-end pressure-time profile, reference motor – straight cylinder, 5.09 cm port diameter – acceleration nullified

Figure 4-7 shows the same SRM, but this time, the accelerative effects on the burning rate were included in the computations. The results indicate again a reduction in both the limit pressure wave amplitude, of about 5.5 MPa (vs. 10.8 MPa for the case of Fig 4-3) and the accompanying base pressure rise of 2 MPa (vs. 5 MPa for the case of Fig 4-3). Nonetheless, DC shift behavior is thus still quite evidently present. The aforementioned decrease in the base pressure and pressure wave amplitude is believed to be due, at least in part, to a smaller propellant surface deflection and corresponding acceleration level, arising from the reduced propellant web thickness.

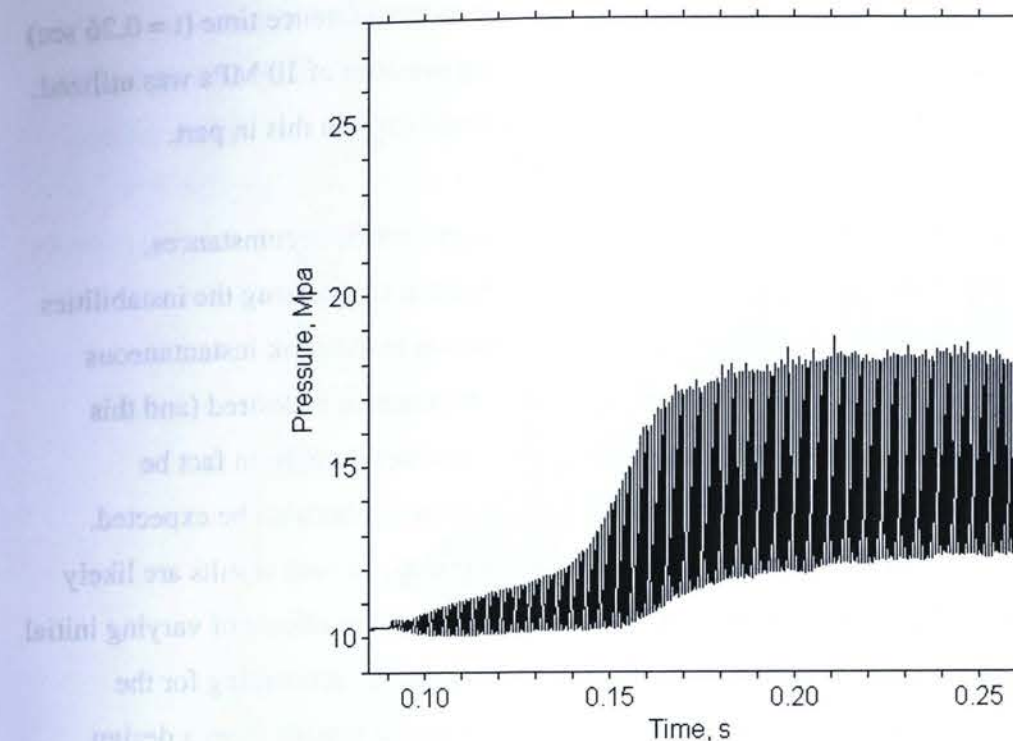


Figure 4-7: Predicted head-end pressure-time profile – straight cylinder, 5.09 cm port diameter – acceleration effect active

Finally, as a side study, the effect of varying the starting chamber pressure was verified, by changing the nozzle throat diameter, while keeping all the other parameters constant. Only two such cases were run, as this effect was only of ancillary interest, largely outside of the scope of the grain area transitions investigation presented in this thesis. The study was performed on the SRM of Figure 4-7, including the accelerative effects in the computations, for starting base pressures of about 8 MPa and 12 MPa. As evidenced by Figure 4-8, increasing the initial chamber pressure to 12 MPa, by decreasing the nozzle throat diameter while keeping all the other parameters constant, resulted in a drastic decrease in the limit pressure wave magnitude to about 1 MPa, as compared to 5.5 MPa for the case of Figure 4-7. A higher base pressure results in a higher base burning rate, which can significantly reduce burning augmentation due to Z-N transient response, flow velocity, and acceleration. This may explain to some degree the above result.

In contrast, changing the starting base pressure to 8 MPa, by increasing the nozzle throat diameter, resulted in a very rapid development of DC shift (see Figure 4-9). However,

somewhat surprisingly, the limit pressure wave magnitude at the reference time ($t = 0.26$ sec) of 4.9 MPa was actually slightly lower than when a starting pressure of 10 MPa was utilized. A lower exit port-to-throat area ratio on wave reflection might explain this in part.

The results are interesting in that they demonstrate that under certain circumstances, increasing the starting chamber pressure might actually result in suppressing the instabilities that would otherwise be present, and consequently, a reduction in the peak instantaneous chamber pressure and casing stress. Hence, if optimum performance is desired (and this means high p_c and as low a casing mass as is structurally feasible) it might in fact be preferable to run at a higher design chamber pressure than would otherwise be expected. However, care must be taken when interpreting the above results, as such results are likely motor-dependent. Nonetheless, a more thorough investigation of the effects of varying initial chamber pressure on combustion instability of a solid rocket motor, accounting for the unsteady and acceleration-driven effects, might be of considerable benefit from a design perspective.

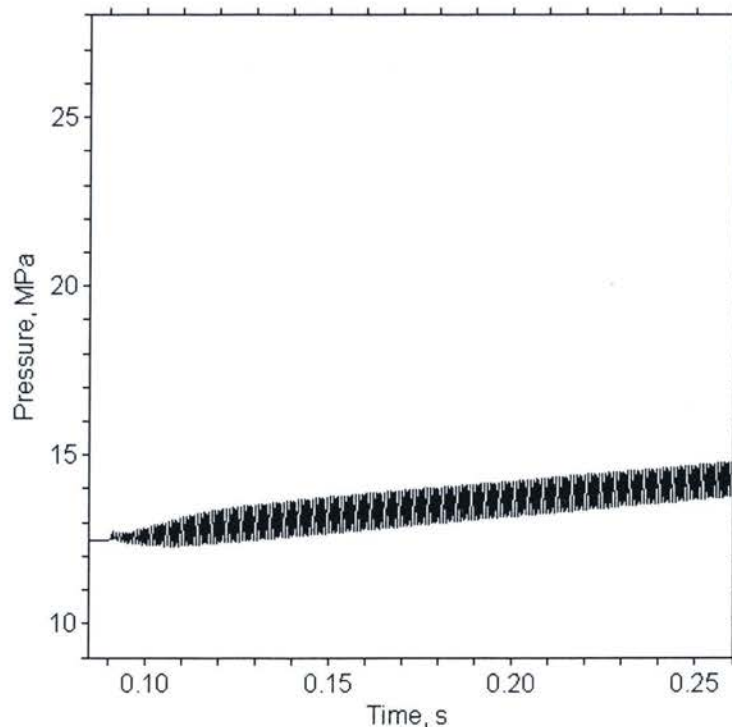


Figure 4-8: Predicted head-end pressure-time profile – straight cylinder, 5.09 cm port diameter – starting pressure 12.1 MPa - acceleration effects active

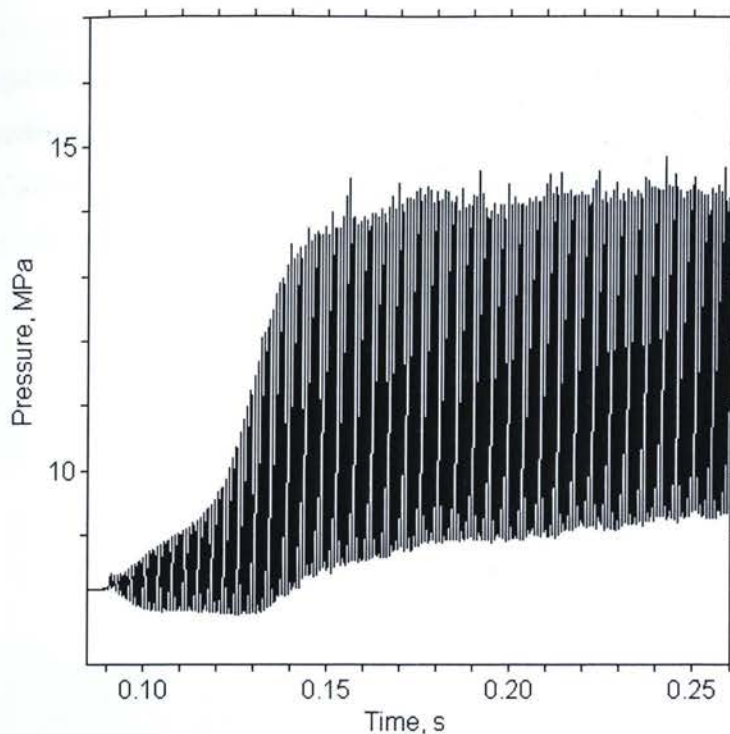


Figure 4-9: Predicted head-end pressure-time profile – straight cylinder, 5.09 cm port diameter – starting pressure 7.95 MPa - acceleration effects active

4.3 Effect of Grain Area Transition Aspect Ratio

In this section, it will be shown that grain port area transitions can, depending on the transition aspect ratio and location, have a significant role in suppressing axial combustion instability in solid rocket motors. An example of a predicted pressure profile for the reference SRM with a shallow transition is presented in Figure 4-10. In this case, the transition is a left-to-right grain port area contraction of a 1.25:1 aspect ratio – that is, the upstream port diameter (by the head end) is 4.03 cm, while the downstream port diameter is 3.6 cm, as per the reference SRM. Length of the transition was set to be 30% of the propellant grain length L_p , in order to represent an area transition with a moderate steepness. The transition midpoint is located at 40% of the grain effective acoustic length ($0.4L$), with the head end being the zero-reference position. The $0.4L$ position was chosen to illustrate the results in this section (as opposed to the chamber midpoint) as it provided for the greatest range of pressure variation as a function of transition aspect ratio. Effects of normal (i.e., radial) acceleration on the burning rate have been included in this particular computation, and in the following results, unless otherwise indicated.

As can be seen from Figure 4-10, the pressure-time profile is qualitatively somewhat similar to the straight-cylinder reference SRM, with a DC shift being very evident. However, as compared to the reference case of Figure 4-3, the limiting pressure wave magnitude is 7.1 MPa, as compared to 10.8 MPa for the reference case, while the rise in base burning pressure has been reduced from well over 5 MPa to about 3.5 MPa.

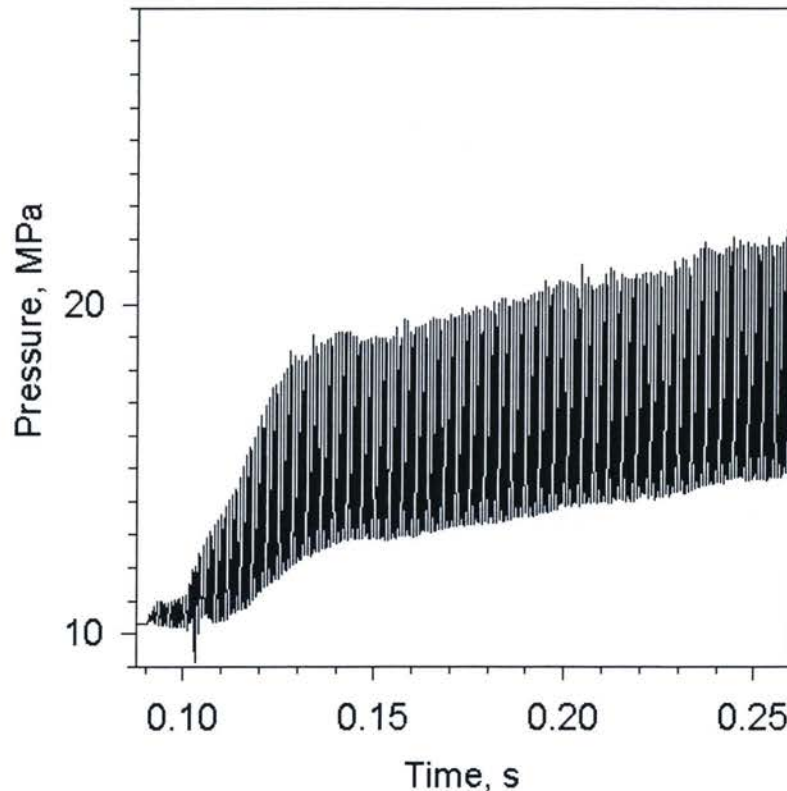


Figure 4-10: Predicted head-end pressure-time profile – 1.25:1 contraction at grain position 0.4L – acceleration active

Increasing the transition aspect ratio to 1.5:1, by changing the port diameter at the head end to 4.41 cm, while keeping all the other parameters unchanged (except for the throat area, which was adjusted to give the same starting pressure of approximately 10.0 MPa, so that the results can be more appropriately compared) results in a qualitatively different pressure-time profile, as illustrated in Figure 4-11. The limit pressure wave magnitude has been reduced to only 0.73 MPa, with a notable lack of any indication of base pressure rise occurring. While the results of Figure 4-11 do include the effects of normal acceleration on the burning rate,

the chamber pressure variation with time is more reminiscent of Figure 4-1, where accelerative effects were omitted (in fact, the wave magnitude is about half of what it was for the case of Figure 4-1).

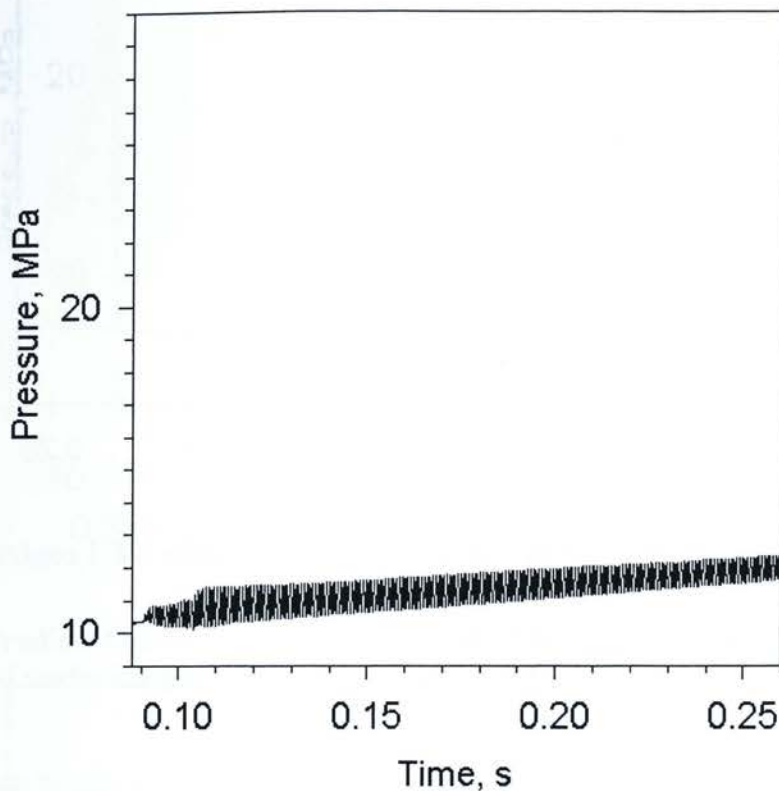


Figure 4-11: Predicted head-end pressure-time profile – 1.5:1 contraction at grain position 0.4L – acceleration active

Effects of a further increase of the port area contraction aspect ratio at the same location, to 2:1 and 2.5:1, are illustrated in Figures 4-12 and 4-13, respectively. It can be seen that the axial pressure wave activity is now almost completely suppressed.

Figure 4-14 shows the results of the same computations in the form of pressure-wave profiles, for four different transition aspect ratios. It can be seen in the case of 1.25 a steep shock front, characteristic of DC-shift dominated behavior is evident, while for the 1.5:1 contraction, the pressure wave has almost a sinusoidal profile. In case of the two higher transition aspect ratios, the wave profile appears to be almost a flat line – with no evidence (regardless of the scale of the chart) of a sustained sinusoidal wave within the resolution of the numerical solver.

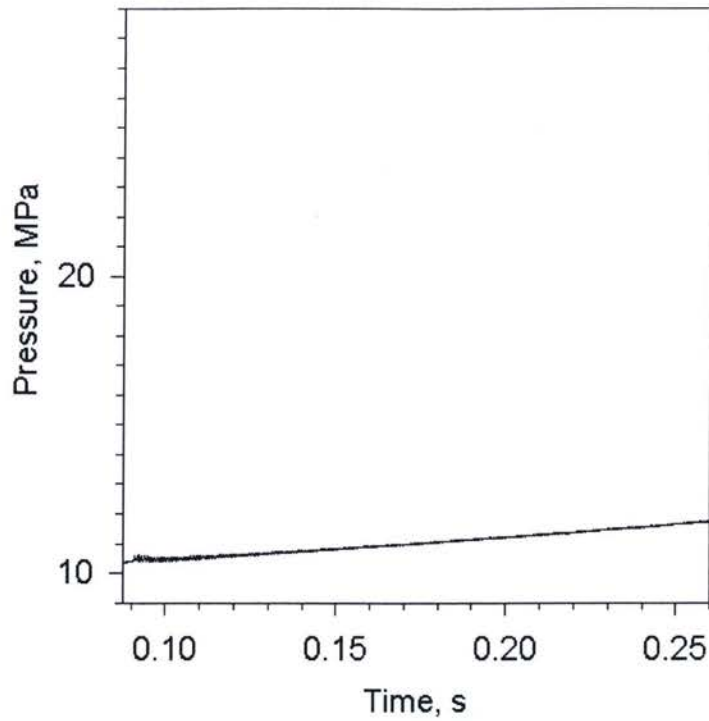


Figure 4-12: Predicted head-end pressure-time profile – 2:1 contraction at grain position 0.4L – acceleration active

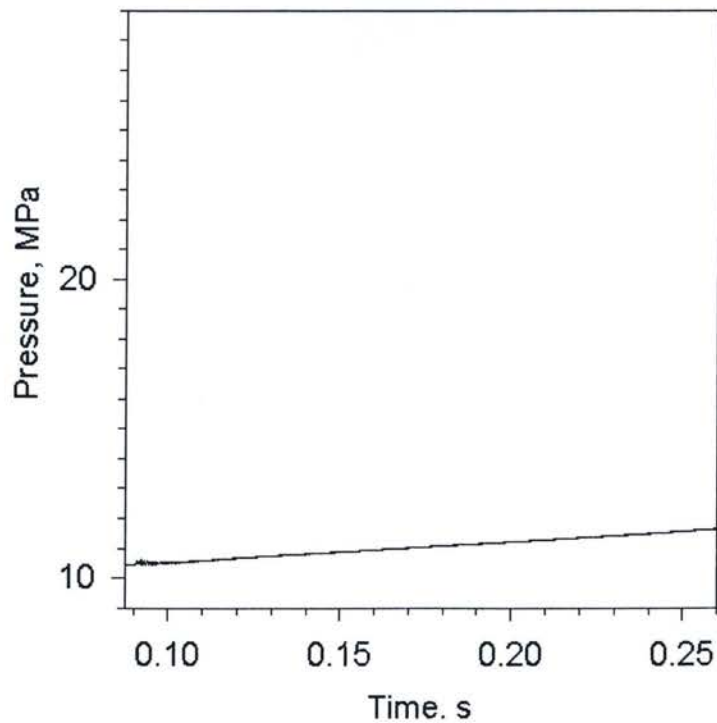


Figure 4-13: Predicted head-end pressure-time profile – 2.5:1 contraction at grain position 0.4L – acceleration active

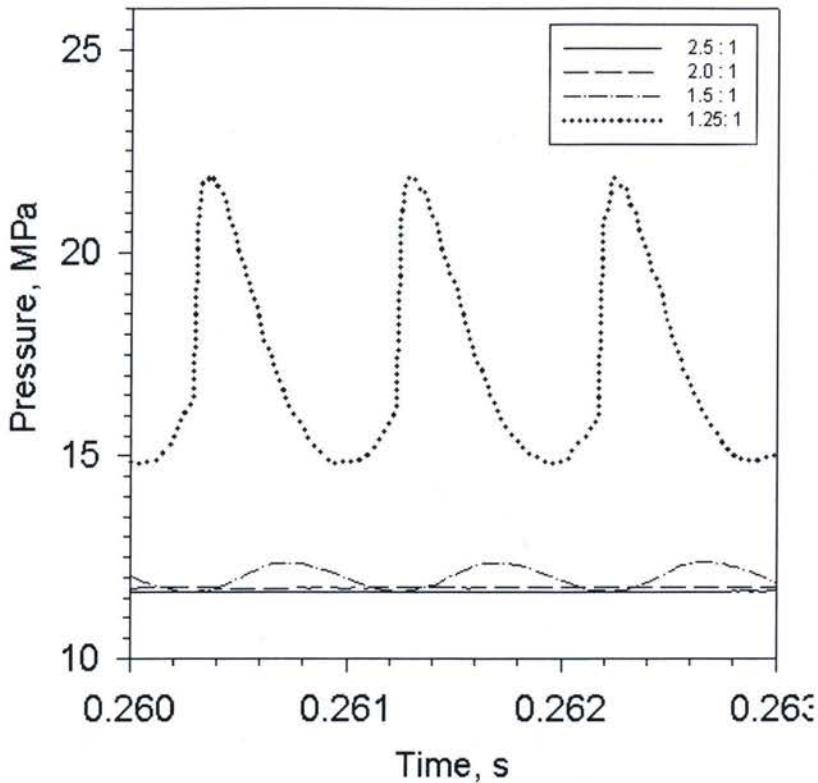


Figure 4-14: Predicted head-end pressure-wave profile for grain port area contractions of various aspect ratios - grain position 0.4L – acceleration active

Similar trends can be observed for left-to-right grain port area expansion (3.6 cm port diameter at the head end, increasing downstream to a value dependent on the transition aspect ratio). Figure 4-15 illustrates the results for a 1.5:1 expansion, located at the 0.4L motor station. Once again, DC shift behavior can be observed, with a limit pressure wave magnitude of 12.9 MPa. It is noted this value is higher than for the reference motor – although the corresponding value near the nozzle end of the grain is somewhat smaller at about 10.5 MPa (see Figure 4-16). It is also noted that a grain contraction of the same aspect ratio of 1.5:1 was shown to reduce the oscillations to only 0.73 MPa (referring back to Figure 4-11), suggesting that grain port area contractions are much more effective at suppressing axial combustion instability than comparable grain port area expansions.

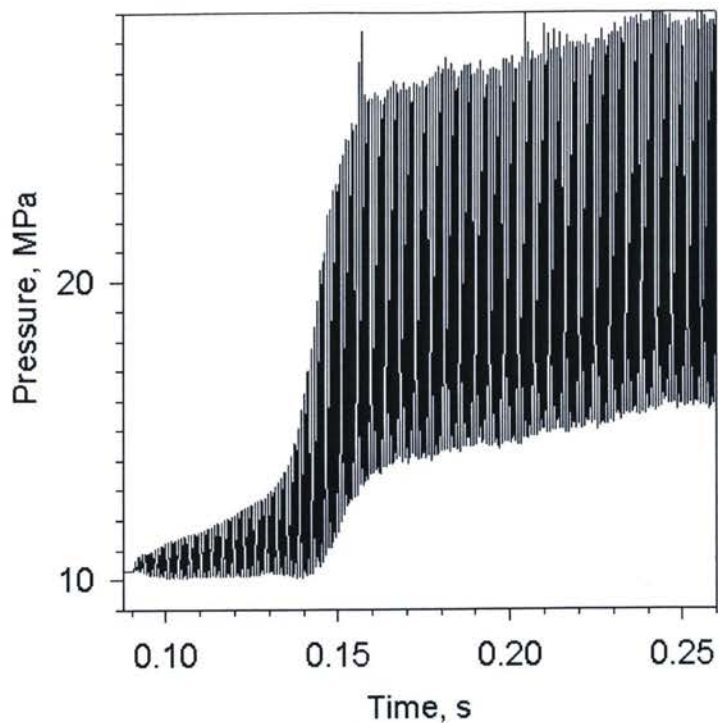


Figure 4-15: Predicted head-end pressure-time profile -1.5:1 expansion at grain position 0.4L - acceleration active

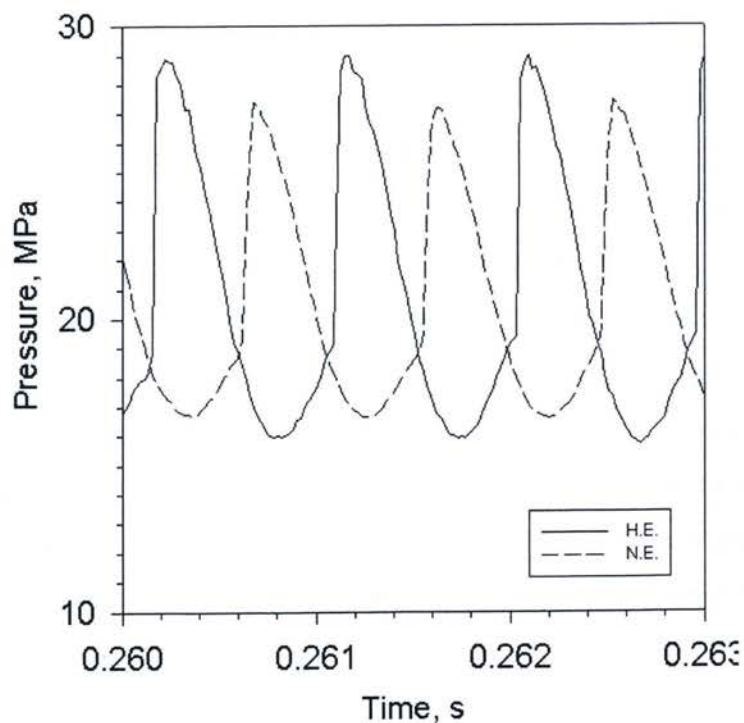


Figure 4-16: Comparison of head-end and nozzle-end pressure-wave profiles -1.5:1 expansion at grain position 0.4L - acceleration active

In contrast, a grain port area expansion of a 1.75:1 aspect ratio was shown to suppress the axial wave magnitude to 1.34 MPa, with no discernable evidence of a DC shift being present (see Figure 4-17). The pressure wave profile was sinusoidal, with a somewhat higher magnitude at the head end, relative to the grain end on the nozzle side, as shown in Figure 4-18. Of interest is the very abrupt change in behavior going from an expansion aspect ratio of 1.5:1 to 1.75:1 – a nearly order-of-magnitude difference in terms of pressure wave amplitude.

Further increasing the expansion aspect ratio to 2:1 (Figure 4-19) and 2.5:1 (Figure 4-20) was shown to increase the degree of instability suppression, although not as effectively as was the case for grain port area contractions. It is noted that in case of the 2.5:1 computation, the code operates on the verge of its solution stability limit, as evidenced by the artificially induced oscillations in the middle section of the curve. A comparison of the four pressure-wave profiles, for the different grain port area expansion aspect ratios is shown in Figure 4-21.

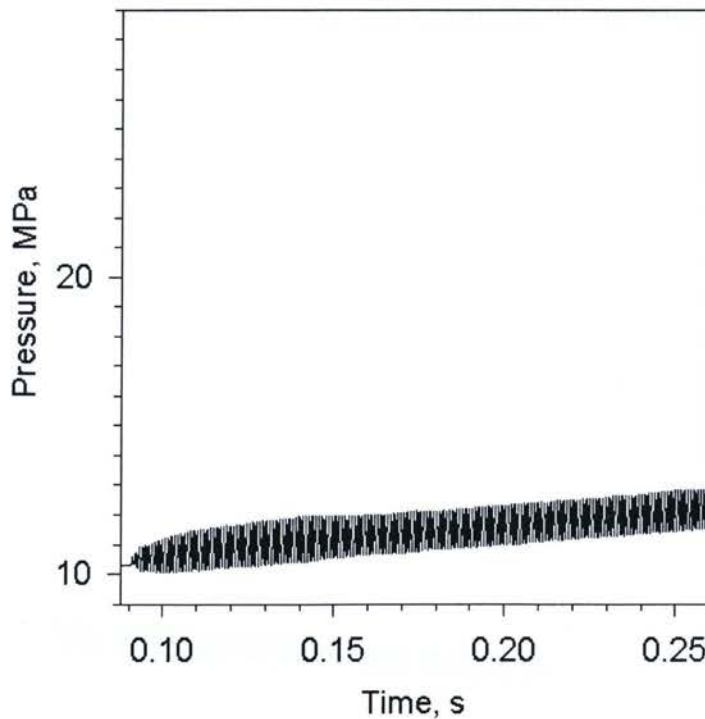


Figure 4-17: Predicted head-end pressure-time profile –1.75:1 expansion at grain position 0.4L – acceleration active

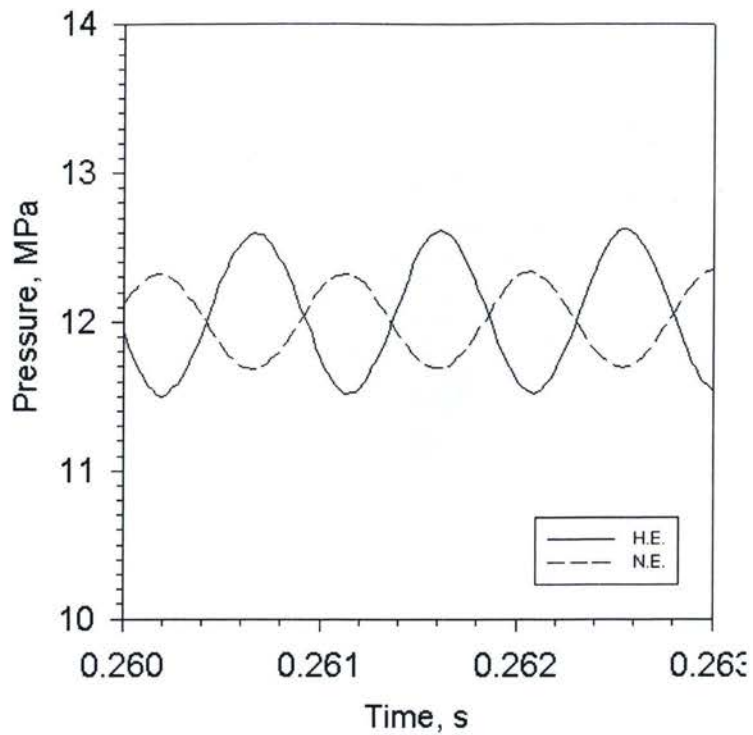


Figure 4-18: Comparison of head-end and nozzle-end pressure-wave profiles -1.75:1 expansion at grain position 0.4L – acceleration active

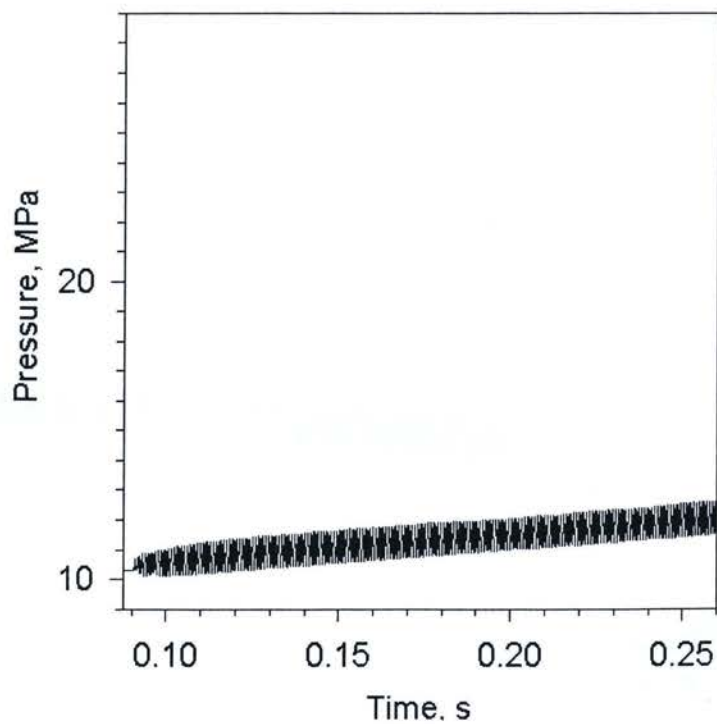


Figure 4-19: Predicted head-end pressure-time profile -2:1 expansion at grain position 0.4L – acceleration active

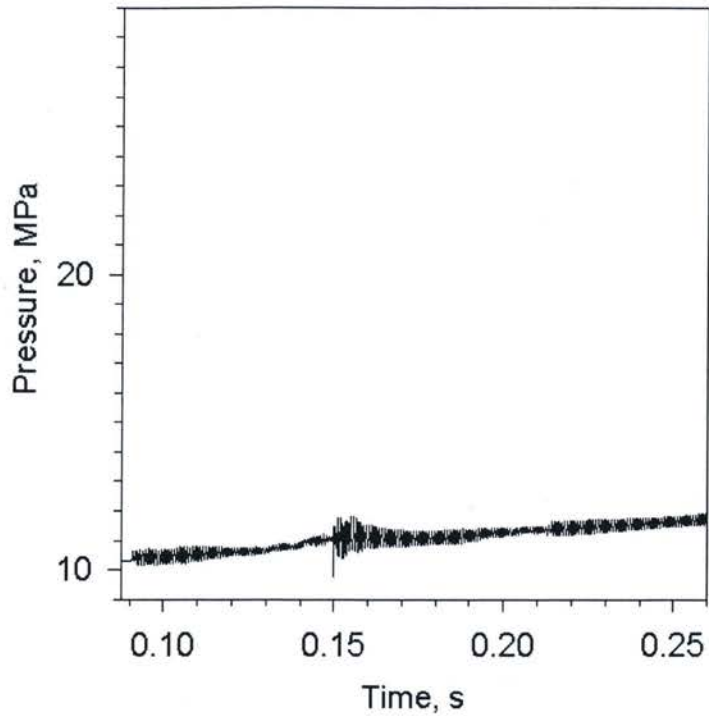


Figure 4-20: Predicted head-end pressure-time profile –2.5:1 expansion at grain position 0.4L – acceleration active

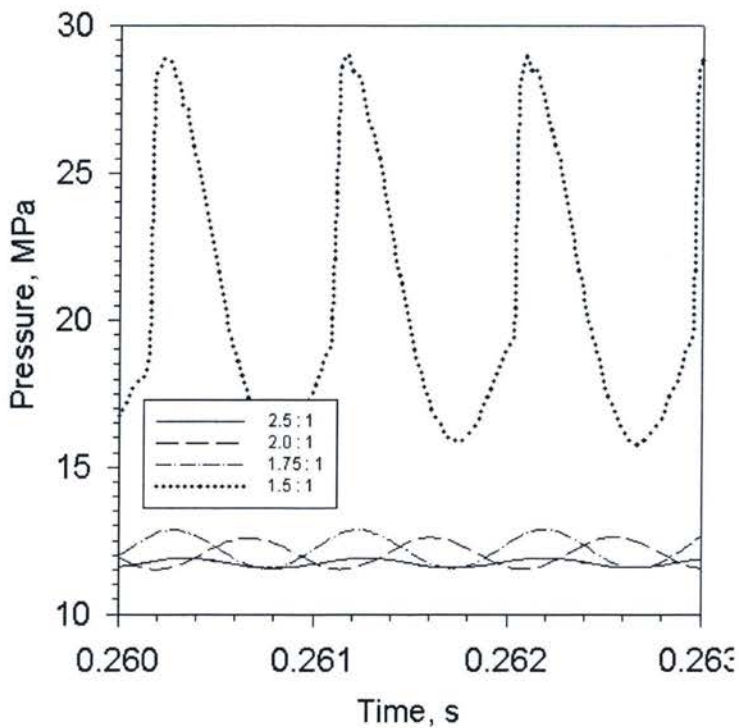


Figure 4-21: Predicted head-end pressure-wave profile for grain port area expansions of various aspect ratios - grain position 0.4L – acceleration active

Figures 4-22 and 4-23 show respectively the effectiveness of the grain port area contraction and expansion. Results are given for both the cases presented where the effect of normal acceleration on the burning rate are included, as well the runs where these accelerative effects were nullified. The effectiveness of the transitions in suppressing the wave activity is expressed in the form of non-dimensional attenuation magnitude:

$$M_a = \frac{\Delta p_{w,peak} - \Delta p_w}{\Delta p_{w,peak}} \quad (44)$$

where Δp_w is the limit pressure wave magnitude (peak-to-trough) for a given simulation, and $\Delta p_{w,peak}$ is the reference zero-suppression pressure wave magnitude (1.42 MPa when acceleration effects are nullified and 10.8 MPa in the case when acceleration effects are included) at the same juncture in the firing (in this case, 0.26 s is the reference time).

As evidenced by Figure 4-22 the effectiveness of a grain port area contraction on suppression of axial wave instabilities is increased with increasing aspect ratio. Similar behavior is predicted regardless whether the effects of normal acceleration on burning rate are included or not, although in the case of accelerative effects included, grain port area contractions of somewhat smaller aspect ratio were shown to have a noticeable effect, in relative terms.

Turning to Figure 4-23 for the expansion cases, it can be observed that increasing the aspect ratio also increases the suppression of axial waves. As compared to grain port area contractions, port area expansions need to have a greater aspect ratio to offer equivalent effect (i.e., they were found to be somewhat less effective than contractions). It is noted that if accelerative effects are nullified, the increase in effectiveness as a function of aspect ratio is somewhat more gradual, as compared to the results where normal acceleration was included.

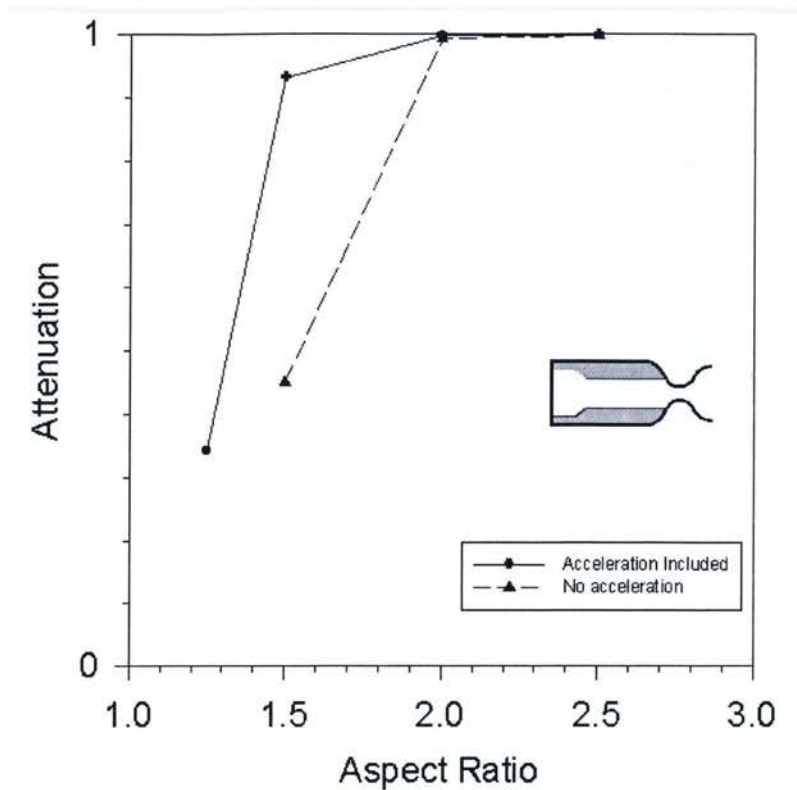


Figure 4-22: Attenuation vs. contraction aspect ratio - grain position 0.4L

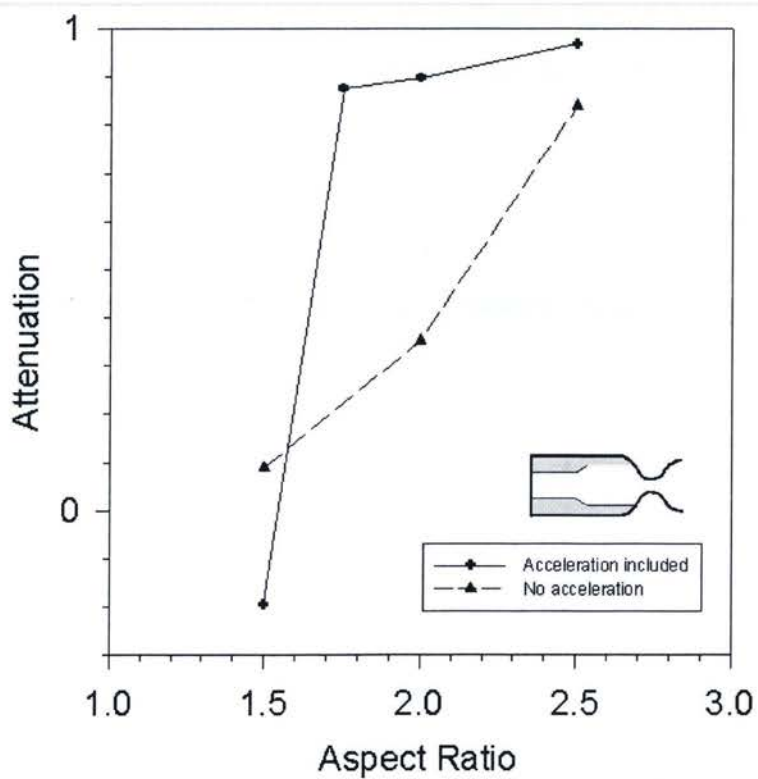


Figure 4-23: Attenuation vs. expansion aspect ratio - grain position 0.4L

The response was also investigated in terms of the predicted level of normal (i.e., radial) acceleration occurring at the sleeve external wall. Figure 4-24 shows the acceleration, expressed in g's, as predicted for the midpoint location of the motor with a 1.5:1 port area expansion located at 0.4L – the time-pressure profile for this motor being given by Figure 4-15. In comparison, Figure 4-25 shows an analogous response for a motor with a port area expansion of 2:1 (pressure-time profile shown in Fig 4-19).

The case of the 1.5:1 expansion exhibits very significant levels of normal acceleration, on the order of 2000-4000 times the acceleration of gravity, while increasing the expansion ratio to 2:1 decreases the acceleration to about 20-40 g's, a two order of magnitude reduction (note the scale of the two charts differs by an order-of-magnitude, for better visibility). It is noted that the level of vibration can therefore be qualitatively correlated to the axial instability behavior in the motor. In particular, the high acceleration levels shown in Figure 4-24 seem to correspond to the DC-shift behavior noted in that particular case. The onset of significant radial vibration activity, occurring at a time just shy of 0.14 seconds, is likely linked to the a very pronounced rise in base pressure that occurs at exactly the same instant in time. Comparing Figures 4-15 and 4-24 it can be seen the vibration level is not proportional to the pressure wave amplitude per se, but appears to be proportional to the degree of the DC shift observed. In contrast, the case of the 2:1 expansion exhibits very moderate radial acceleration levels, and no discernible DC shift.

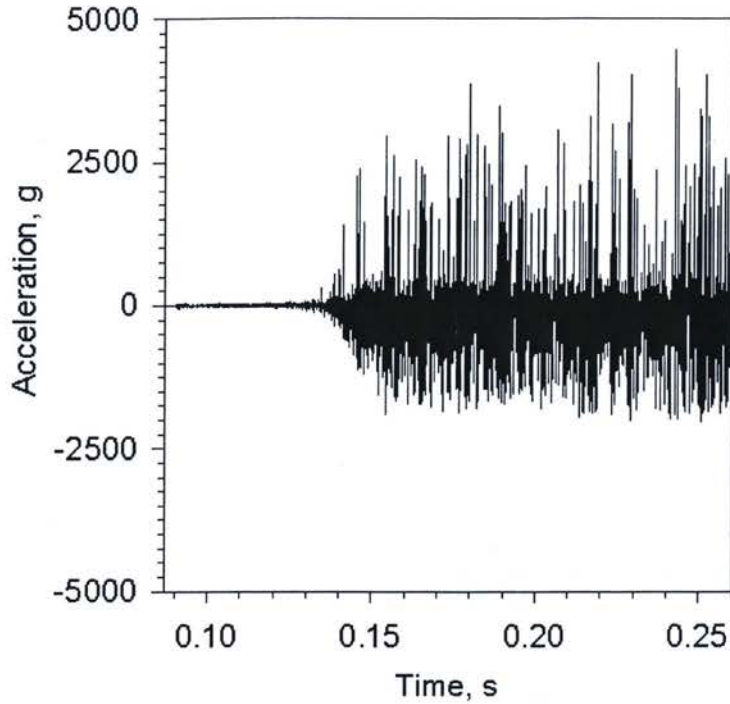


Figure 4-24: Predicted motor-midpoint normal acceleration at the sleeve external surface -time profile -1.5:1 expansion at grain position 0.4L

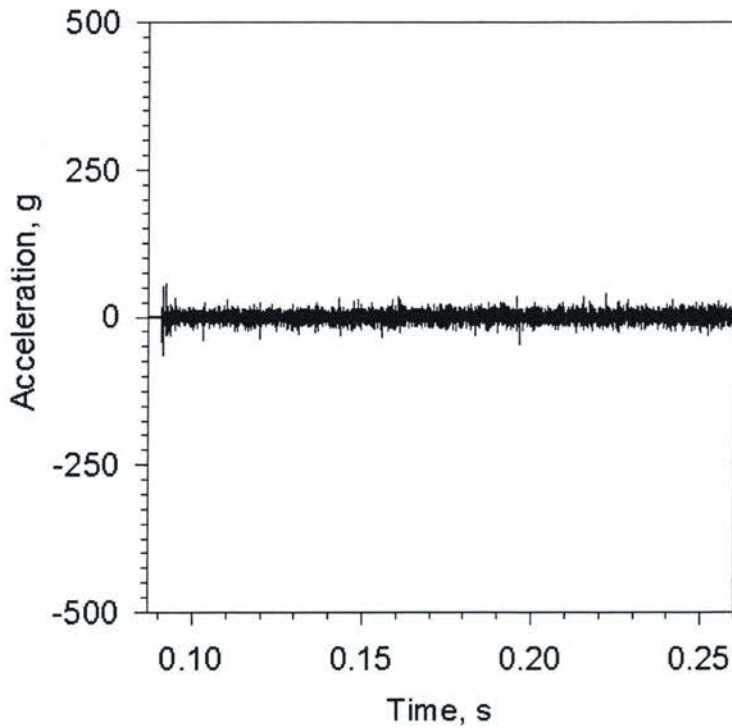


Figure 4-25: Predicted motor-midpoint normal acceleration at the sleeve external surface -time profile -2:1 expansion at grain position 0.4L

To an extent, the above results agree with those obtained experimentally by Koreki et al.¹⁰, where it was found that convergent port configurations (i.e. grain area contractions) were found to suppress combustion instability. The same experimenters found divergent port configurations (i.e. expansions) were not nearly as effective, and had the potential to increase combustion instability, especially when propellant web thickness was large in comparison to the port diameter.

4.4 Effect of Grain Area Transition Position

The effect of the position of the grain port area transition was investigated by performing numerical simulations for transitions located at different motor stations (i.e., at different distances from the head end). Sample results are illustrated in this section, based on the case of a 2:1 port area contractions and expansions. In all cases described in this subsection, the transition length remained set at 30% of the motor grain length (investigation of the effect of changing the transition steepness is described in section 4.6).

Figure 4-26 illustrates the pressure-time profile for a grain port area contraction with its midpoint located at 0.75L, one-quarter motor length away from the nozzle. A limit pressure wave magnitude of 0.88 MPa is noted, which is considerably larger than that determined for the same transition at 0.4L, a value of 0.02 MPa. Thus, in the case of grain area contractions, moving the transition towards the nozzle end of the motor had the effect of reducing its efficiency. The opposite was found to occur for moving the contraction towards the head end of the motor (albeit in the case of this SRM, a contraction located at 0.4L was already suppressing the pressure wave activity fully). For a grain port area expansion example, Figure 4-27 shows the pressure time profile for a 2:1 expansion located near the head end, at 0.25L. The corresponding limiting pressure wave magnitude at the end of the simulation was 1.55 MPa, being somewhat higher than when the expansion was placed at 0.4L. Thus, in contrast to the case of port area contractions, the effectiveness of expansions is found to decrease the closer the expansion is to the motor head end. In all cases for a 2:1 transition (whether expansion or contraction), no evidence of a DC shift was observed for this motor, and the axial pressure wave was about an order of magnitude smaller than for the straight cylinder case.

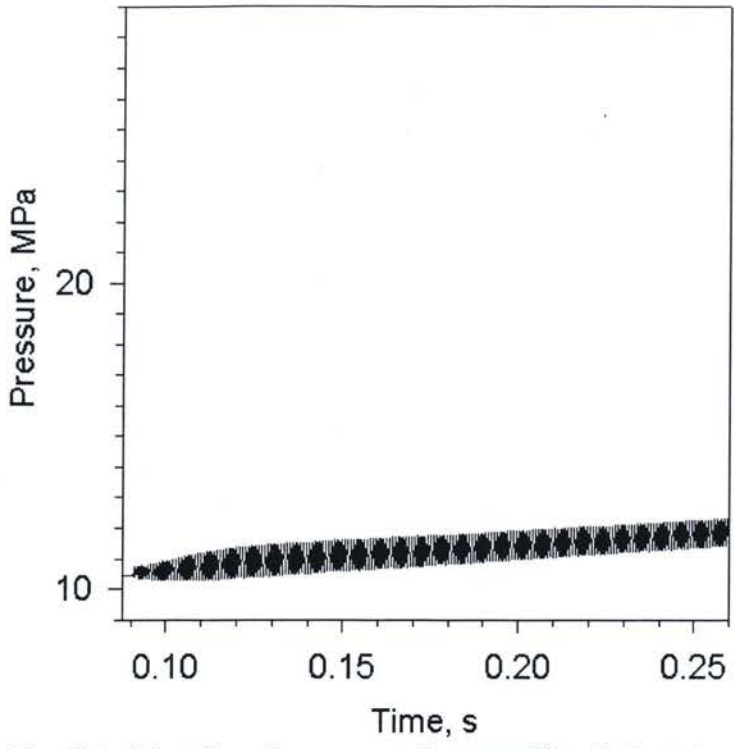


Figure 4-26: Predicted head-end pressure-time profile -2:1 contraction at grain position 0.75L – acceleration active

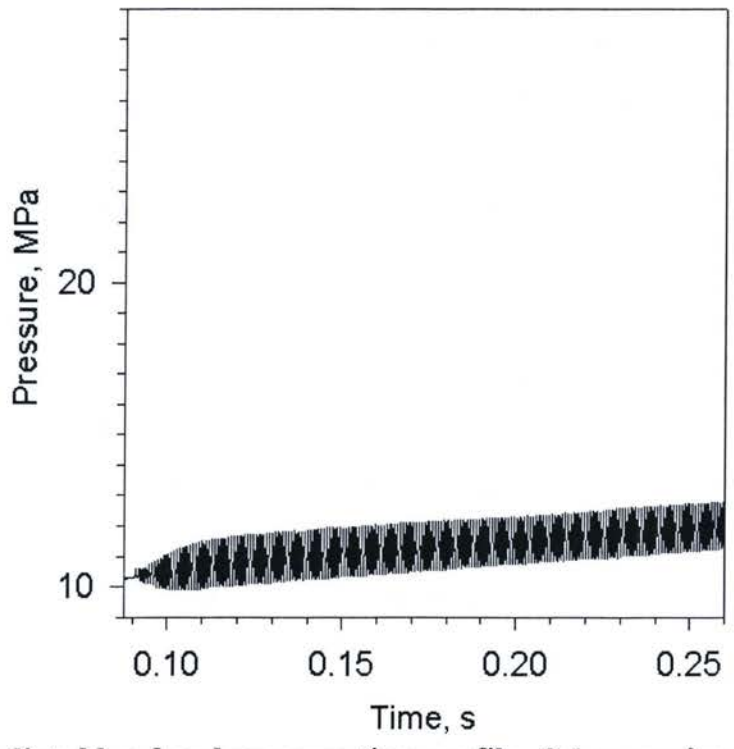


Figure 4-27: Predicted head-end pressure-time profile -2:1 expansion at grain position 0.25 – acceleration active

A more thorough understanding of the results can be obtained by examining the non-dimensional attenuation magnitude as a function of axial position of the transition. Due to the limitations on steepness, the study was largely restricted to area transition midpoint positions between $0.25L$ and $0.75L$. Figure 4-28 shows the attenuation vs. position of the midpoint of the transition (expressed as a fraction of the motor acoustic length) for a 2:1 port area contraction and a 2:1 expansion, in cases where the effects of normal acceleration on the burning rate have been nullified. It is evident that the effectiveness in suppressing axial wave activity of port area contractions decreases as the contraction is moved toward the nozzle end past a certain point (in this case, placing the contraction downstream of the chamber midpoint reduces its effectiveness). The opposite is true for port area expansions which were found to be more effective the closer they were placed to the nozzle end. Note the transition from near zero attenuation to full suppression of wave activity as the position is changed occurs in a rather gradual manner.

Figure 4-29 shows analogous results, but this time with the effects of acceleration on the burning rate included in the computational runs. Once again, the effectiveness of port area contractions was seen to increase as the contraction was moved towards the head end, while effectiveness of expansions was increased by moving them towards the nozzle end. Unlike the acceleration-nullified case, the results of Figure 4-29 show significantly less dependence, magnitude-wise, on the position. For this particular aspect ratio, a transition, whether expansion or contraction, was shown to be fully effective at eliminating the DC shift-dominated behavior, regardless of the position of the transition. The bracket symbol to the right of the expansion curve of Figure 4-29 indicates that substantial variability up and down from the trend curve can be expected in this region. Nonetheless, comparing the results to the contraction case, as well as corresponding results for Figure 4-28, one can expect the general trend to continue, up to expansion position $0.75L$. It is also noted that in spite of the difference in magnitude between Figures 4-28 and 4-29, the inflection points of both sets of curves occur at approximately the same motor axial positions. In fact, if the reference zero-suppression pressure wave magnitude of 1.42 MPa, corresponding to the non-acceleration baseline case, was used for the acceleration-included cases (instead of its baseline value of 10.8 MPa), the two charts would look very similar.

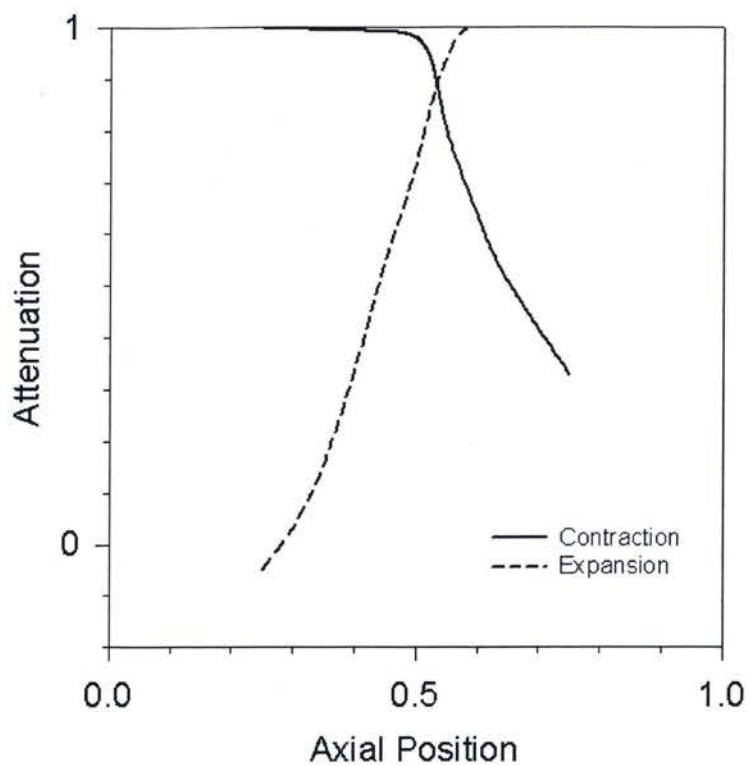


Figure 4-28: Attenuation vs. axial position of transition – acceleration nullified

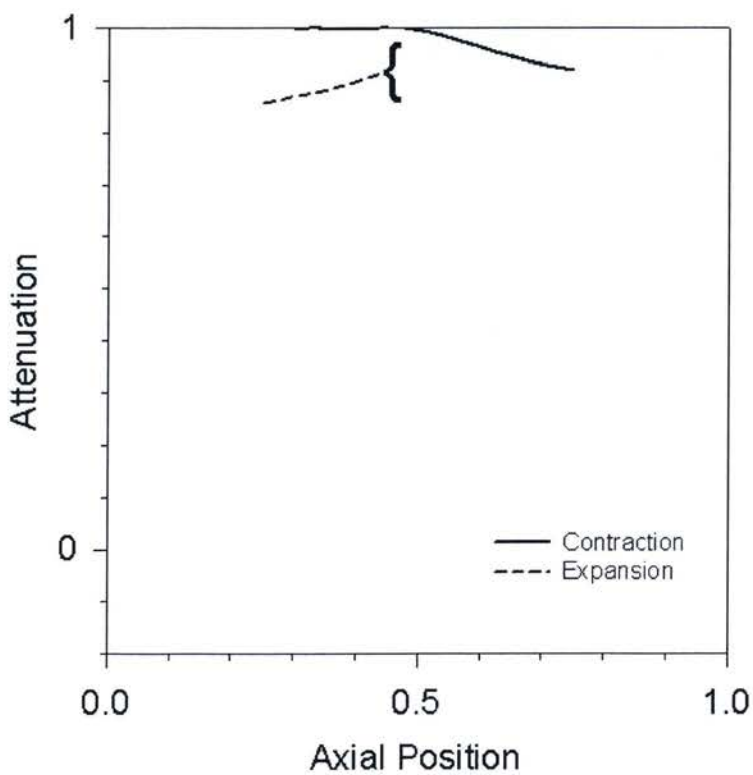


Figure 4-29: Attenuation vs. axial position of transition – acceleration active

4.5 Attenuation Maps

While the two previous sections of this work treated the effect of changing the transition aspect ratio and position separately, the most comprehensive understanding of the results and trends can be obtained by examining the applicable attenuation maps. Figures 4-30 through 4-33 summarize visually the results of over 140 computational runs performed for different transition aspect ratios and positions, for both expansions and contractions, where the effects of acceleration have been either included or nullified. The various M_a curves are displayed as a function of non-dimensional axial position (x/L) of the grain transition (given the area transition has a relatively shallow slope as required for a quasi-one-dimensional flow model, with the transition length being set at 30% of the grain length, the midpoint of the transition is the reference location), with each curve being at a particular area contraction or expansion ratio. The x -axis in essence represents the straight-cylinder case (no suppression at any axial position). The brace (curly bracket) symbol represents regions where substantial variability up or down from the trend curve can be expected.

The following observations can be made:

- Increasing the transition aspect ratio tends to increase the transition's effectiveness in suppressing pressure wave activity. This is true for both port area expansions and contractions, regardless of whether the effect of normal acceleration on the burning rate was accounted for or not.
- Moving a grain contraction closer towards the head end of the motor tends to increase its effectiveness. This was found to be the case regardless if accelerative effects were included.
- In contrast, moving a grain expansion closer towards the nozzle end of the motor tends to increase its effectiveness. Again, this was found to be the case regardless if accelerative effects were included.

- A significant behavioral difference was observed depending on whether effects of normal acceleration on the burning rate were included or not. If acceleration was nullified, the effect of moving the transition, and to a lesser extent, changing its aspect ratio, was rather gradual or moderate, in terms of the attenuation obtained. In contrast, where accelerative effects were accounted for, it was observed that two very distinct regions of behavior were observed:
 - A DC-shift dominated region, characterized by high pressure wave magnitude (low attenuation), and a base pressure rise – occurring at low transition aspect ratio.
 - Region where evidence of DC shift is absent, corresponding to moderate and high transition aspect ratios.
- Where accelerative effects were included, no case was observed where a shift from one region to the other could occur simply by moving the transition. However, based on up-and-down variability observed in some runs, it is believed the system tends to either one or the other distinct equilibrium states, and a bifurcation analysis is required to understand this behavior more fully.
- It is also noted that discounting the cases where DC shift occurs, and using non-acceleration zero-attenuation reference wave magnitude for the acceleration-included cases, would result in the acceleration-included curves being very close to the acceleration-nullified curves. This reinforces the fact that the presence of the DC shift is explicitly linked to the radial vibration of the propellant.

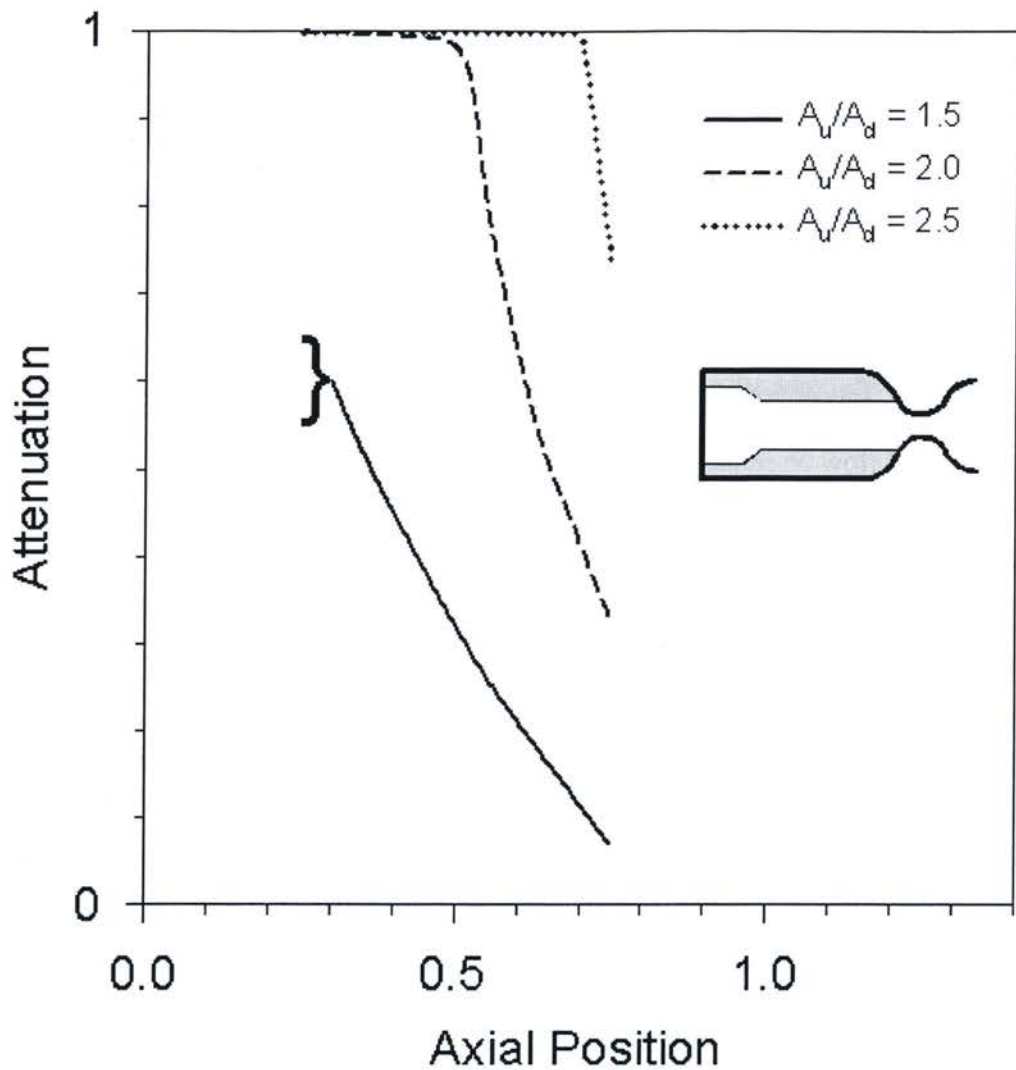


Figure 4-30: Attenuation map: grain contraction, acceleration nullified, ref. time at $t = 0.26$ s, initial pressure disturbance of 2 atm, transition length of 0.156 m (36 cells, 30% of grain length)

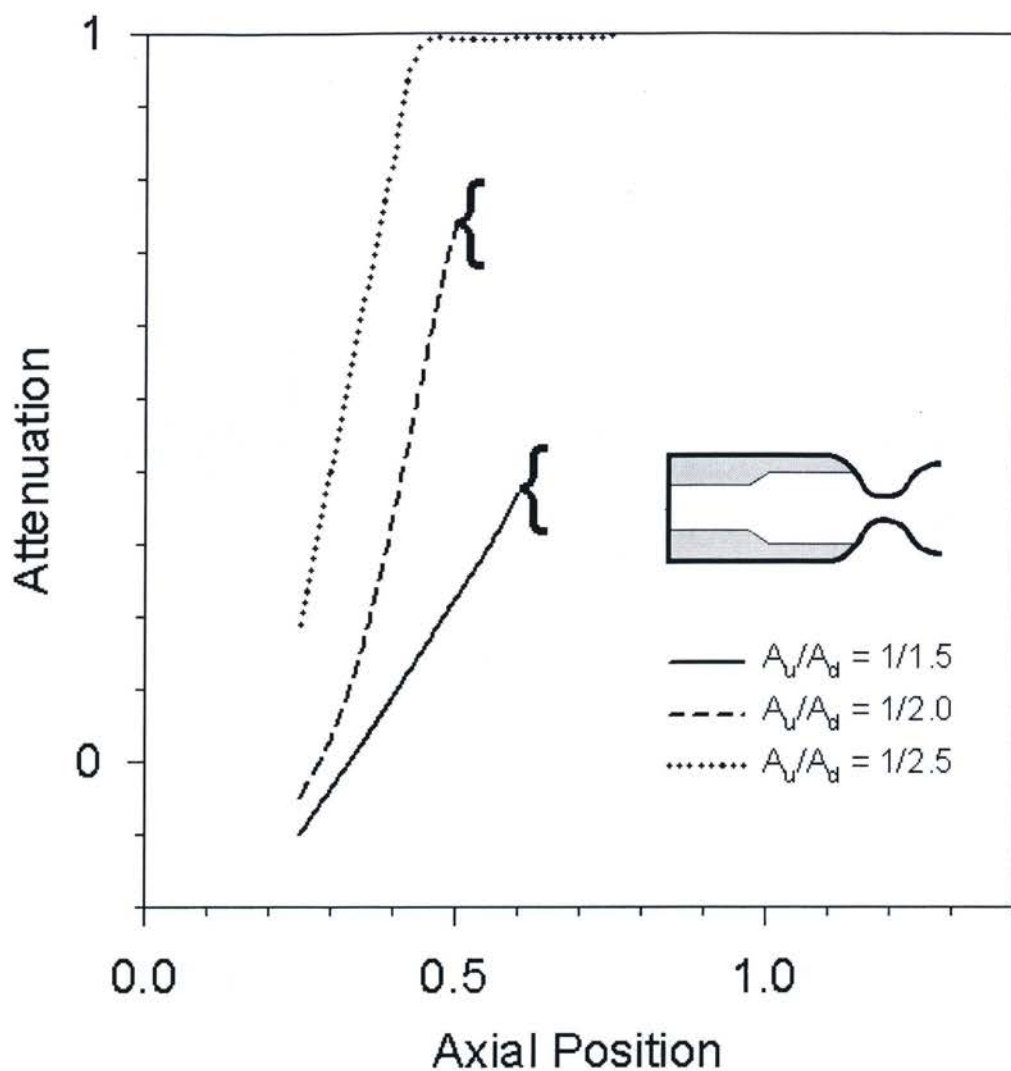


Figure 4-31: Attenuation map: grain expansion, acceleration nullified, ref. time at $t = 0.26$ s, initial pressure disturbance of 2 atm, transition length of 0.156 m (36 cells, 30% of grain length)

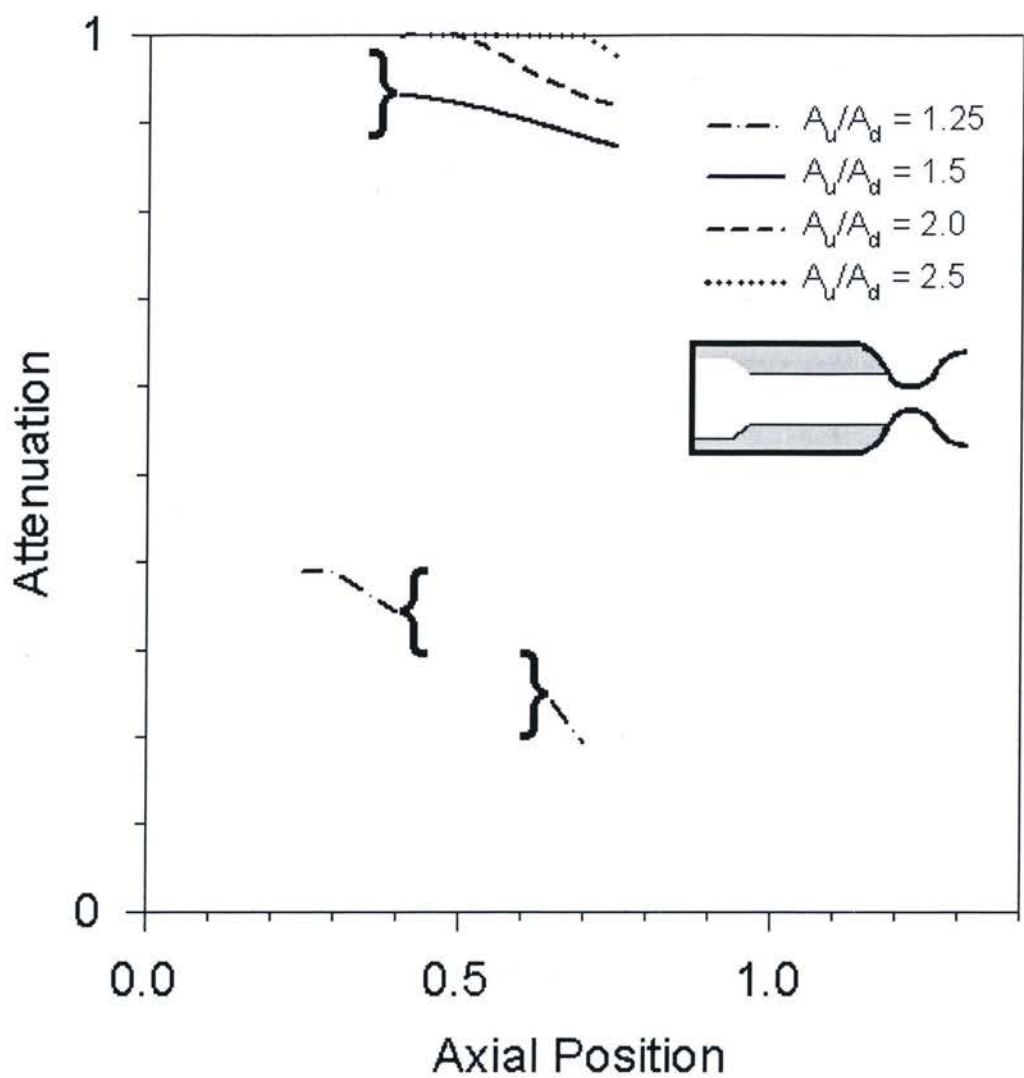


Figure 4-32: Attenuation map: grain contraction, acceleration active, ref. time at $t = 0.26$ s, initial pressure disturbance of 2 atm, transition length of 0.156 m (36 cells, 30% of grain length)

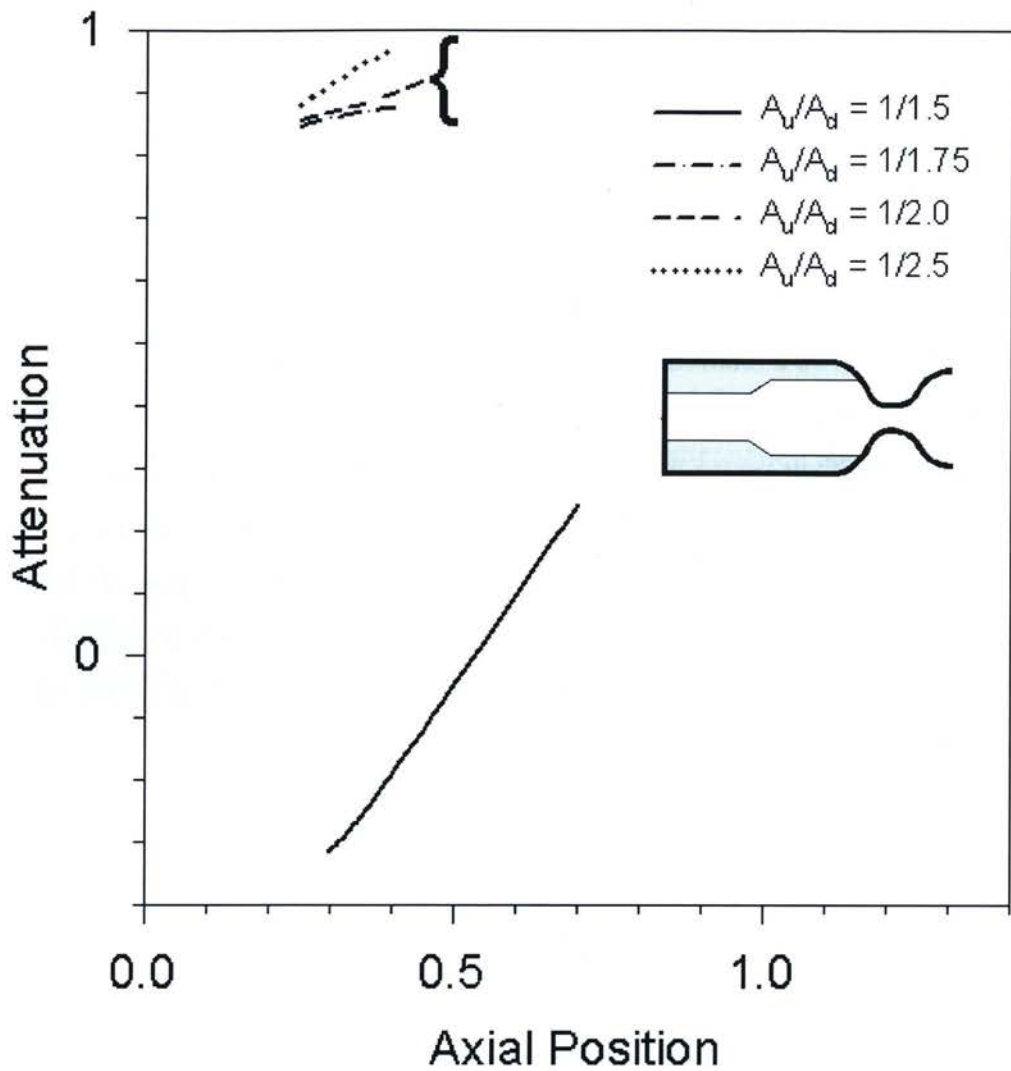


Figure 4-33: Attenuation map: grain expansion, acceleration active, ref. time at $t = 0.26$ s, initial pressure disturbance of 2 atm, transition length of 0.156 m (36 cells, 30% of grain length)

4.6 Effect of Transition Steepness

The effect of transition steepness was investigated by performing computations for varying values of transition length. The case of a 2:1 port area expansion was chosen for the study, located at the 0.45L location along the motor chamber (i.e. near the midpoint, slightly closer to the head end).

Figure 4-34 shows a relationship between the transition length, expressed as a fraction of the overall grain length L_t/L_p , and the resulting non-dimensional attenuation magnitude M_a . Accelerative effects on the burning rate were nullified for the initial study. As can be seen from Figure 4-34, increasing the transition steepness results in a significant increase in its effectiveness, for the reference motor studied. In particular, a 2:1 grain expansion of a length equal to 15% of the grain length or less, results in nearly a complete suppression of axial pressure wave activity. In contrast, a transition length of about half the length of the grain shows negligible attenuation.

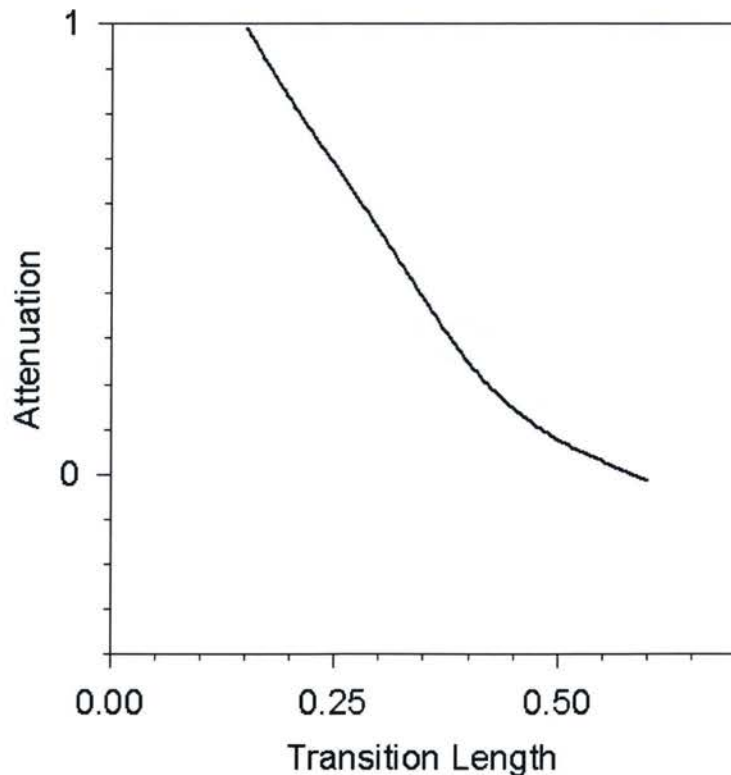


Figure 4-34: Attenuation vs. transition length – 2:1 expansion - acceleration nullified

The foregoing study was repeated with accelerative effects now accounted for. As evidenced by Figure 4-35, expansion lengths of $0.35L$ or less resulted in a significant reduction of pressure wave activity, the effectiveness becoming more pronounced the shorter the transition. However, for transition lengths of $0.5L$ or more, no suppression of pressure waves was noted (attenuation being slightly negative, due to the larger port cross-sectional area relative to the baseline case of constant 3.6 cm port diameter), the rise in base pressure (DC shift) being quite pronounced. Although no runs were successfully completed for expansion lengths in-between $0.4L$ and $0.5L$, based on prior evidence and the shape of the curve in Figure 4-35, it is believed that the transition between the no-attenuation and the high-attenuation regions is quite abrupt – the dashed line in Figure 4-35 represents a region of numerical instability. In physical terms, a 2:1 expansion located at $0.43L$ is not expected to result in attenuation of 0.5 , but rather, is expected to exhibit either the DC-shift-dominated behavior, or a relatively high attenuation of above 0.8 , if indeed an equilibrium solution is obtained.

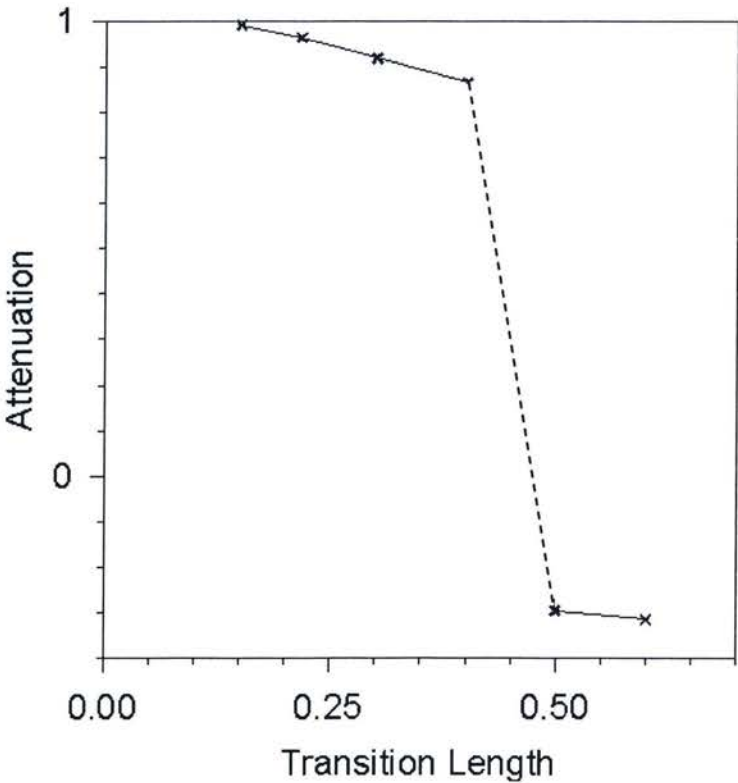


Figure 4-35: Attenuation vs. transition length – 2:1 expansion - acceleration active

Further runs were performed to determine the effectiveness of varying the length of the 2:1 port area expansion, at different locations along the grain. Figure 4-36 shows the effect of changing the position along the grain of 2:1 port area expansions of three different lengths. As before, moving the port area expansion closer to the nozzle end results in an increase in its effectiveness. It is noted that in case of a very shallow expansion ($L_t/L_p = 0.6$) positioning it closer to the nozzle beyond $0.55L$ results in a decrease in attenuation (trending to the zero axis), while positioning it closer to the head end below $0.3L$ appears to have the curve trending to the 5.09-cm straight cylinder result, as one might expect in the limiting case.

The corresponding results where accelerative effects were accounted for, are found in Figure 4-37. The behavior is similar to that noted for the acceleration-nullified runs, except that the most shallow expansion is dominated by the DC-shift behavior, regardless of its position, with correspondingly a very low degree of attenuation.

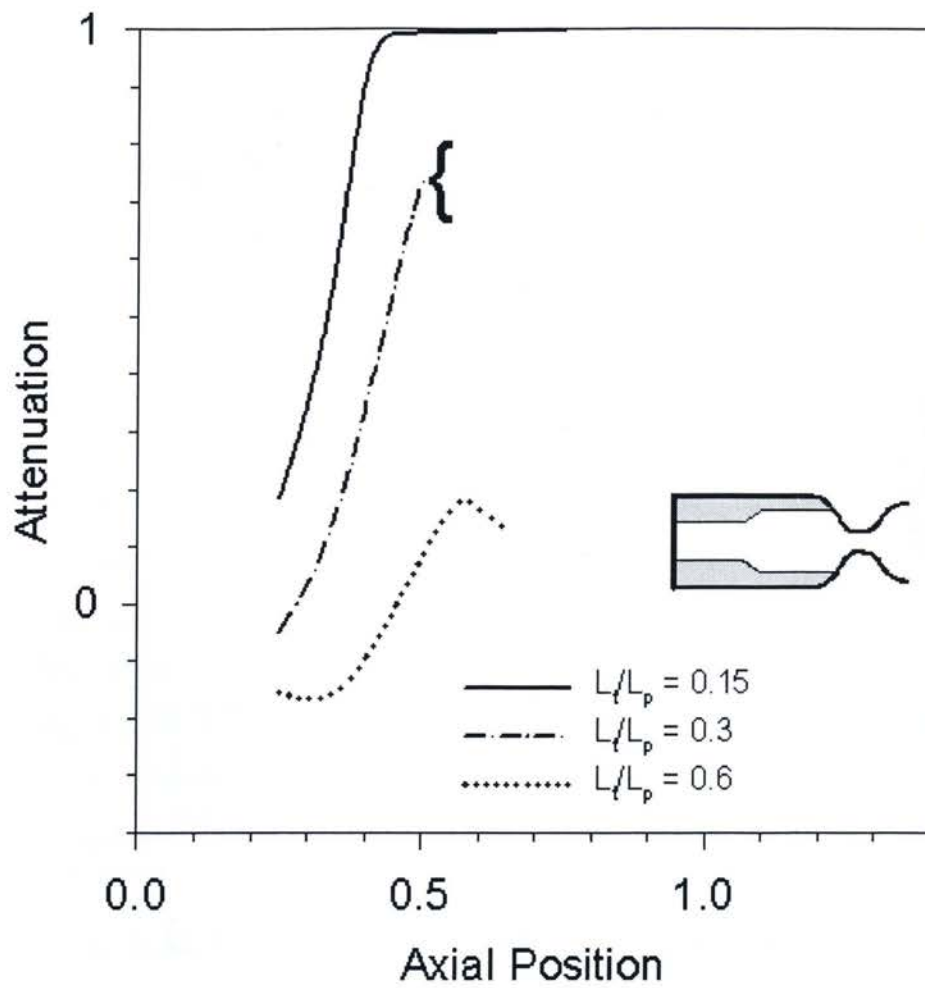


Figure 4-36: Attenuation map: grain 2: 1 expansion, acceleration nullified, ref. time at $t = 0.26$ s, initial pressure disturbance of 2 atm

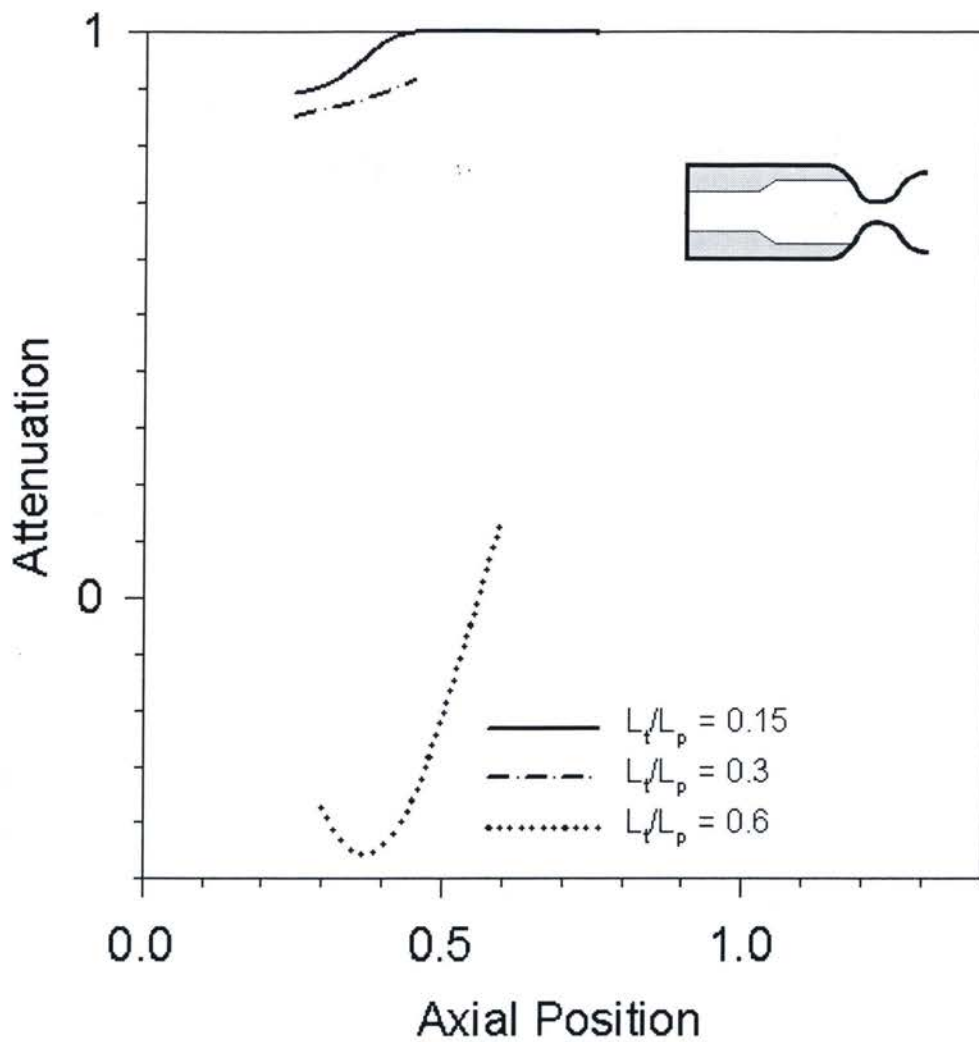


Figure 4-37: Attenuation map: grain 2: 1 expansion, acceleration active, ref. time at $t = 0.26$ s, initial pressure disturbance of 2 atm

5 Conclusion

5.1 Final Remarks

The effectiveness of grain port area transitions as a means for suppression of axial combustion instability in solid rocket motors has been demonstrated. It was found that the effectiveness of the transition depends on the transition type (contraction vs. expansion), aspect ratio, position of the transition along the grain, and finally, the steepness of the transition. In particular:

- Increasing the transition aspect ratio tends to increase its effectiveness in suppressing pressure wave activity, for both port area expansions and contractions.
- Moving a grain contraction closer towards the head end of the motor tends to increase its effectiveness.
- Moving a grain expansion closer towards the nozzle end of the motor tends to increase its effectiveness.
- Increasing the steepness of a transition results in an increase in its effectiveness.

In addition, it was found that the behavior differed somewhat depending whether the effects of normal acceleration on the burning rate were included or not, in that acceleration-included cases have shown a rather rapid change from a flow regime characterized by the presence of the DC-shift phenomenon to a more gradual linear-instability regime, as the transition parameters were varied.

5.2 Recommendations for Future Work

A given limitation of this work was the focus on only a single basic grain configuration and propellant type. Significantly more computations would have to be performed to verify to what extent the trends established here hold for completely different motor/propellant configurations.

In the end, numerical computations can only take us so far – one should rely as much as possible on correlation of numerical data with experimental data. Thus, opportunity exists for parametric studies of the effectiveness of grain area transitions using hot-flow rocket motor experiments. While such investigations are by their very nature, quite expensive, they can and would prove to be invaluable in forming the basis of a more comprehensive approach for prediction and suppression of combustion instability symptoms in motors utilizing grain port area transitions and other suppression techniques.

In terms of a refined prediction of propellant inner-surface vibration, a more refined 2D axisymmetric or 3D structural model would be of benefit to a future study. Care however must be exercised when employing finite element analysis to this purpose, as material characterization should ideally allow for a nearly incompressible formulation, perhaps by the use of hyper-elastic material properties. As of this date, computational resources are a major barrier to the employment of such an approach, given the high number of computational runs required to develop trend charts for all the various parameters at play.

Finally, the usage of a 2D axisymmetric or 3D flow solver model would enable simulations of steeper, and hence, potentially more effective, grain area transitions than those presented in this document.

References

- ¹Oberg, C.L., Haymes, W.G., and Wong, T.L., "Solid Propellant Combustion Instability Suppression Devices", AIAA Paper. No. 72-1051, Nov. 29-Dec.1, 1972.
- ²Colucci, S.E., "Mechanical Suppression Devices to Stabilize Solid Rocket Motors", AIAA Paper. No. 73-1222, Nov. 5-7, 1973.
- ³Price, E.W., "Solid Rocket Combustion Instability – An American Historical Account", in: De Luca, L., Price, E.W. and Summerfield, M., eds., *Nonsteady Burning and Combustion Stability of Solid Propellants*, Progress in Astronautics & Aeronautics series, Vol. 143, AIAA Publications, Washington DC, 1992, pp. 1-16.
- ⁴Brownlee, W.G., "Nonlinear Axial Combustion Instability in Solid Propellant Motors", *AIAA Journal*, Vol. 2, No. 2, Feb. 1964, pp. 275-284.
- ⁵Barrère, M., "Introduction to Nonsteady Burning and Combustion Instability", in: De Luca, L., Price, E.W. and Summerfield, M., eds., *Nonsteady Burning and Combustion Stability of Solid Propellants*, Progress in Astronautics & Aeronautics series, Vol. 143, AIAA Publications, Washington DC, 1992, pp. 17-58.
- ⁶Culick, F.E.C., "Prediction of the Stability of Unsteady Motions in Solid-Propellant Rocket Motors", in: De Luca, L., Price, E.W. and Summerfield, M., eds., *Nonsteady Burning and Combustion Stability of Solid Propellants*, Progress in Astronautics & Aeronautics series, Vol. 143, AIAA Publications, Washington DC, 1992, pp. 719-780.
- ⁷Fishbach, S.R., Majdalani, J. and Flandro, G.A., "Acoustic Instability of the Slab Rocket Motor", *Journal of Propulsion & Power*, Vol. 23, No. 1, Jan.-Feb. 2007, pp. 146-157.
- ⁸Kooker, D.E. and Zinn, B.T., "Triggering Axial Instabilities in Solid Rockets: Numerical Predictions", AIAA Paper. No. 73-1298, Nov. 5-7, 1973.
- ⁹Baum, J.D. and Levine, J.N., "Modeling of Nonlinear Longitudinal Instability in Solid Rocket Motors", *Acta Astronautica*, Vol. 13, No. 6/7, 1986, pp. 339-348.
- ¹⁰Koreki, T., Aoki, I., Shirota, K. and Toda, Y., "Experimental Study on Oscillatory Combustion in Solid-Propellant Rocket Motors," *Journal of Spacecraft & Rockets*, Vol. 13, No. 9, Sept. 1976, pp. 534-539.
- ¹¹Golafshani, M., Farshchi, M. and Ghassemi, H., "Effects of Grain Geometry on Pulse-Triggered Combustion Instability in Rocket Motors," *Journal of Propulsion & Power*, Vol. 18, No. 1, Jan.-Feb. 2002, pp. 123-130.
- ¹²Sanal Kumar, V.R., Kim, H.D., Raghunandan, B.N., Setgouchi, T. and Raghunathan, S., "Diagnostic Investigation of Instabilities and Pressure Oscillations in High-Performance Solid Rockets," AIAA Paper No. 2005-3999, July 10-13, 2005.

¹³Greatrix, D.R., "Suppression of Axial Combustion Instability in Solid Rocket Motors," Computational Ballistics III, proceedings by WIT Press, pp. 57-66, The New Forest, U.K., June 6-8, 2007.

¹⁴Greatrix, D.R. and Harris, P.G., "Structural Vibration Considerations for Solid Rocket Internal Ballistics Modeling", AIAA Paper No. 2000-3804, July 17-19, 2000.

¹⁵Loncaric, S., Greatrix, D.R. and Fawaz, Z., "Star-Grain Rocket Motor — Nonsteady Internal Ballistics", *Aerospace Science & Technology*, Vol.8, No. 1, Jan. 2004, pp. 47-55.

¹⁶Montesano, J., Behdinan, K., Greatrix, D.R. and Fawaz, Z., "Internal Chamber Modeling of a Solid Rocket Motor: Effects of Coupled Structural and Acoustic Oscillations on Combustion," *Journal of Sound & Vibration*, Vol. 311, No. 1-2, Mar. 18, 2008, pp. 20-38.

¹⁷Greatrix, D.R. and Gottlieb, J.J., "Higher-Order Random Choice Method for Internal Ballistic Flows", 7th Annual Conference of the CFD Society of Canada (*CFD99*), May 30-June 1, 1999.

¹⁸Ben-Artz, M. and Falcovitz, J., "An Upwind Second Order Scheme for Compressible Duct Flows", *SIAM Journal on Scientific & Statistical Computing*, Vol. 7, No. 3, July 1986, pp.774-768.

¹⁹Brewster, M.Q., "Solid Propellant Combustion Response: Quasi-Steady (QSHOD) Theory Development and Validation", in: Yang, V., Brill, T.B. and Ren, W.Z., eds., *Solid Propellant Chemistry, Combustion, and Motor Interior Ballistics*, Vol. 185, Progress in Astronautics and Aeronautics, AIAA, 2000, pp. 607-638.

²⁰Greatrix, D.R., "Transient Burning Rate Model for Solid Rocket Motor Internal Ballistic Simulations", *International Journal of Aerospace Engineering*, Vol. 2008, Article 826070, 2008, pp. 1-10.

²¹Greatrix, D.R., "Numerical Modeling Considerations for Transient Burning of Solid Propellants", AIAA Paper No. 2005-4005, July 10-13, 2005.

²²Greatrix, D.R., "Transient Solid-Propellant Burning Rate Model: Comparison to Experimental Data", AIAA Paper No. 2006-4426, July 9-12, 2006.

²³Greatrix, D.R., "Particles for Instability Suppression in Solid Rocket Motor", AIAA Paper No. 2007-5804, July 8-11, 2007.

²⁴Greatrix, D.R., "Model for Prediction of Negative and Positive Erosive Burning", *Canadian Aeronautics & Space Journal*, Vol. 53, No. 1, Mar. 2007, pp. 13-21.

²⁵Greatrix, D.R., "Parametric Analysis of Combined Acceleration Effects on Solid-Propellant Combustion", *Canadian Aeronautics and Space Journal*, Vol. 40, No. 2, June 1994, pp. 68-73.

²⁶Popov, E.A., *Mechanics of Materials*, 2nd ed., Prentice-Hall, New Jersey, 1976.

²⁷Hoffmann, K.A. and Chiang, S.T., *Computational Fluid Dynamics for Engineers*, Vol. 1, Engineering Education System, Wichita, 1993.